The Effect of Matrix Shear Strength on the out-of-plane Compressive Strength of CFRP Cross-ply Laminates

B. Yu [a], S.N. Khaderi [b], V.S. Deshpande [a], N.A. Fleck [a 1]

[a] *Department of Engineering, University of Cambridge, Trumpington St., Cambridge, CB2 1PZ, UK*

[b] *Department of Mechanical and Aerospace Engineering, Indian Institute of Technology Hyderabad, Ordnance Factory Estate, Yeddumailaram - 502 205, Telangana, India*

27 December 2017

Abstract

The failure mechanism of 'indirect tension' is explored for cross-ply IM7/8552 carbon fibre/epoxy laminates subjected to quasi-static, out-of-plane compressive loading. The sensitivity of compressive response to strain rate and to the state of cure is measured, motivated by the hypothesis that the out-of-plane compressive strength is sensitive to the matrix shear strength. A pressure-sensitive film is placed between specimen and loading platen, and reveals that a shear lag zone of reduced compressive traction exists at the periphery of the specimen, giving rise to a size effect in compressive strength. The width of the shear lag zone reduces with increasing shear strength of the matrix. The laminates fail by the indirect tension mechanism: out-of-plane compressive loading generates tension in the fibre direction for each ply and ultimately induces fibre tensile failure. Finite element (FE) simulations and an analytical model are developed to account for the effect of matrix shear strength, specimen geometry, and strain rate on the out-of-plane compressive strength. Both the FE simulations and the analytical model suggest a recipe for increasing the through-thickness compressive strength.

Keywords: Composite materials, Laminates, Out-of-plane compression, Failure mechanism, Shear lag, Strain-rate sensitivity, rate-dependent response, Finite element, Indirect tension

Submitted to International Journal of Solids and Structures, December 2017

[1] Corresponding author. Tel.: +44-1223-332650; fax: +44-1223-332662. E-mail address: naf1@eng.cam.ac.uk

1 Introduction

Attwood et al. (2014) have recently demonstrated that Dyneema® cross-ply composites fail by the mechanism of 'indirect tension' under out-of-plane compressive loading; this failure mechanism in fibre composites was originally proposed by Woodward et al. (1994). Unidirectional Dyneema® has an extremely low value of shear strength, and it is unclear whether a low shear strength is required in order to trigger this failure mechanism. Attwood et al. (2014) showed that the indirect tension mechanism in cross-ply laminates is a consequence of the differing lateral expansions of the $0°$ and $90°$ plies. The argument is as follows. Consider a stack of alternating $0°$ and $90°$ plies and subjected to out-of-plane compressive loading in the *z*-direction by a uniform pressure p, see Fig. 1a. A unit cell consists of a single $0°$ ply (labelled A in Fig. 1a) adhered to an underlying $90°$ ply (labelled B). If the two plies were allowed to slide freely with respect to each other, then ply B would undergo a much larger Poisson expansion in the *y*-direction than ply A, due to the orientation-dependent Poisson's ratio. This relative motion is prevented by adhesion between the two layers, and the two layers share the same strain in the *y*-direction. Layer A is subjected to a tensile stress σ_{yy}^{A}, whereas layer B experiences a compressive stress $\sigma_{yy}^{B} = -\sigma_{yy}^{A}$, to satisfy no net force in the *y*-direction. Additionally, by a symmetry argument, $\sigma_{xx}^{B} = \sigma_{yy}^{A}$ and $\sigma_{xx}^{A} = \sigma_{yy}^{B}$. The purpose of the present study is to explore the extent to which indirect tension is an active failure mechanism for carbon fibre/epoxy cross-ply laminates. The sensitivity of the indirect tension mechanism to the matrix shear strength is determined by considering laminates in various states of cure.

The precise relationship between the in-plane stress state in a specimen of finite size and the applied pressure p is dependent upon the choice of constitutive law for each ply but, in broad terms, the in-plane stresses are of similar magnitude to the applied pressure p. Additionally, interlaminar shear occurs at the inter-layer between the alternating $0°$ and $90°$ plies in a shear-lag zone near the periphery of the specimen. Within this shear lag zone (of characteristic length l_s), the pressure p and in-plane stresses build up from the outer edge of the specimen towards the centre, see Fig. 1c. The pressure p remains uniform at a maximum value of $p_{\max}$ within the central region; the magnitude of $p_{\max}$ increases as the compressive strain $-\varepsilon_{zz}$ rises and failure occurs by tensile in-plane fibre rupture. This mechanism has been

analysed previously by Attwood et al. (2014) for a rate-independent, elasto-plastic composite response. In the present study, we shall develop a detailed analysis for the rate-dependent case.

Attwood et al. (2014) found that the out-of-plane compressive strength of the cross-ply laminates scales with the tensile strength of the fibres, thereby suggesting that the ballistic resistance of a composite can be increased by using fibres of higher tensile strength. O'Masta et al. (2015), Karthikeyan et al. (2013) and Attwood et al. (2016) subsequently confirmed that the ballistic resistance of Dyneema® cross-ply composites is dictated by the in-plane tensile failure of plies. The role of matrix shear strength in influencing the ballistic strength is less clear. Preliminary experiments by Karthikeyan et al. (2013) suggest that matrix shear strength does have a significant effect on the ballistic resistance of carbon fibre reinforced plastic (CFRP). We note in passing that the indirect tension mechanism is fundamentally different from the membrane-stretching mode of Phoenix and Porwall (2003).

In the present study, we shall explore in detail the role of matrix cure upon the mechanism of indirect tension for quasi-static out-of-plane compression of IM7/8552 carbon fibre/epoxy cross-ply composites. Particular attention is paid to the effect of rate sensitivity of the matrix upon the out-of-plane strength. In a typical out-of-plane compression test on a cross-ply laminate, the pressure $p_{\max}$ is sufficiently high (on the order of 1 GPa) that the attendant high values of hydrostatic stress leads to a significant change in the shear strength of the matrix and in the tensile strength of the fibres. These interactions are included in our analysis. In summary, a combined experimental, numerical, and analytical study is given in order to address the role of specimen geometry (thickness-to-width ratio) and state of cure upon the observed out-of-plane compressive strength of the CFRP cross-ply laminates.

1.1 Strain Rate and Pressure Sensitivity

The strain rate sensitivity of the matrix flow strength in composites is evident in tests employing dynamic loading or a hot-wet environment, as noted *inter alia* by Daniel et al. (1981), Gates and Sun (1991), Soutis and Turkmen (1997), Staab and Gilat (1995), and Sun and Chen (1989). Commonly, rate sensitivity of the matrix is characterised by a rate-dependent power law, see for example Gates and Sun (1991), Slaughter et al. (1993), and Week and Sun (1998).

The shear strength of the polymeric matrix in a fibre reinforced composite is also pressure dependent. Collings (1974) observed that the out-of-plane compressive strength of a unidirectional (UD) ply in CFRP is significantly higher than the out-of-plane tensile strength. He also noted that shear bands formed at an angle of $30°$ to the compressive loading axis, instead of $45°$ as commonly seen in the shear yielding of metals. He concluded that the yield strength of the epoxy matrix is pressure-dependent. Collings' work motivated a number of studies on the transverse compression of UD plies with superimposed hydrostatic pressure, see for example Hine et al. (1999, 2005), Pae and Rhee (1995) and Zinoviev and Tsvetkov (1998). In general, it was observed that the yield strength of the composites increases with superimposed hydrostatic pressure. The underlying idea is that the fibres remain elastic, and slide past each other in the manner of a granular flow, with plastic deformation of the intervening polymeric matrix. A Mohr-Coulomb law is commonly used to account for the pressure sensitivity of yield strength of the composite ply, along with non-associated flow, see for example Argon et al. (1968), González and LLorca (2007), Rabinowitz et al. (1970), Ward (1971).

Now consider the sensitivity of fibre tensile strength to hydrostatic stress. Hine et al. (1999) found that the tensile strength of dry carbon fibre tows decreases with an increase in superimposed pressure. Similarly, the in-plane tensile strength of carbon, glass and Kevlar composites (in an epoxy matrix) decreases with increasing superimposed pressure, see for example Parry and Wronski (1985, 1986), Sigley et al. (1991), Zinoviev Tsvetkov (1998) and Hine et al. (1999, 2005). The precise reason for this weakening effect is unclear but the effect is widely recognised, and we shall include it in our analysis.

1.2 Outline of Study

The outline of the present study is as follows. The manufacturing process of $0°/90°$ cross-ply IM7/8552 laminates is described. Out-of-plane compression tests are reported, with pressure-sensitive film used to determine the distribution of contact pressure between the platens and specimens. Fractography is used to confirm that failure is by the indirect tension mechanism. The sensitivity of the indirect tension mechanism to matrix shear strength is measured by considering laminates in various states of cure. Additionally, finite element and analytical models are developed in order to help explain the sensitivity of out-of-plane compressive strength to matrix properties and to specimen geometry.

2 Specimen Manufacture

Cross-ply laminates of lay-up $[0°/90°]_8$ were laid-up manually from Hexply® 8552/35%/134/IM7 carbon fibre/epoxy prepreg, of ply thickness 0.131 mm. Five states of specimen cure were used, with the following labelling: (A) uncured, (B) partially cured at 100 °C for 2 hours, (C) partially cured at 120 °C for 2 hours, (D) partially cured at 180 °C for 24 hours, and (E) autoclaved and fully cured. The partially cured lay-ups of type (B) to (D) were prepared in a conventional air-oven using the above cure cycles; they were compressed at 0.1 MPa in the out-of-plane direction by spring-loaded platens during the curing process. The fully cured specimens (E) were autoclaved following the usual procedure as recommended by Hexcel Ltd.. With the exception of the fully cured material (E), all laminates were stored at -15 °C prior to testing in order to avoid additional curing.

The matrix shear strength of the laminates in the five states of cure, and over a range of strain rates, was measured using two types of shear test. A tensile test[1] on a $\pm 45°$ lay-up was used to measure the *in-plane* shear strength and a short beam shear test[2] was used to measure the *out-of-plane* longitudinal shear strength of the laminates. The shear test set-ups and results are summarised in Appendix A. In general, the matrix shear strength increases with the state of cure. Laminates in a low state of cure, such as materials (A) and (B), are the most strain rate sensitive and can be characterised by a rate-dependent power-law:

$$\frac{\tau}{\tau_{IP}} = \left(\frac{\dot{\gamma}}{\dot{\gamma}_0} \right)^m, \qquad \text{in-plane shear test} \tag{1a}$$

and

$$\frac{\tau}{\tau_{OP}} = \left(\frac{\dot{\gamma}}{\dot{\gamma}_0} \right)^m, \qquad \text{out-of-plane, longitudinal shear test.} \tag{1b}$$

Here, τ is the shear stress corresponding to any shear strain rate $\dot{\gamma}$. The exponent *m* is found to be the same for both the in-plane and out-of-plane responses, and so only a single value is reported in Table 1 for each of materials (A) and (B). $\dot{\gamma}_0$ is a reference shear strain rate (taken to be $\dot{\gamma}_0 = 10^{-3}\text{s}^{-1}$), τ_{IP} is the *in-plane* shear strength at a given shear strain (taken here to be

[1] In accordance to ASTM A3518.
[2] In accordance to ASTM A2344.

γ = 5%), and τ_{OP} is the out-of-plane longitudinal shear strength (again at γ = 5%). In contrast, materials (C) to (E), in high states of cure, are almost rate insensitive. For materials (C) to (E), the in-plane shear yield strength, as measured from the $\pm 45°$ tensile test (τ at γ = 5%), is comparable to the longitudinal shear strength, as measured from the short beam shear tests (taken from the peak shear stresses), see Table 1.

3 Out-of-plane Compression Tests

The cross-ply specimens $[0°/90°]_8$ of thickness 2 mm (16 plies) and of side length $L \times L$ (with L in the range of 3 mm to 15 mm) were compressed in the out-of-plane direction (see Fig. 1b) between two hardened silver steel platens (700 Vickers), using a screw-driven test machine with a 150 kN load cell. The platens were lubricated with a low viscosity mineral oil to reduce friction to a negligible level. The compression tests were performed at three selected values of out-of-plane strain rate: $-\dot{\varepsilon}_{zz} = 8\times10^{-4}\text{s}^{-1}$, $8\times10^{-3}\text{s}^{-1}$, and $8\times10^{-2}\text{s}^{-1}$. For each state of cure, a minimum of 24 specimens were tested to failure for selected values of specimen side length L and strain rate. The compressive load $-F$ was recorded by the machine load cell and the displacement between the steel platens was measured using a laser extensometer.

For selected samples, measurements were made of the pressure distribution (i.e. normal compressive traction) on the loaded face. To achieve this, Fuji Prescale® pressure measurement films[1] were used to map the pressure distribution of the specimens during the compression test. These films were chosen for their fine spatial resolving power (~ 0.2 mm) and large range of pressure measurements (up to 300 MPa). During the compression test, a stack of pressure measurement films[2] was placed between the specimen and the steel platen. Each film contains a colour-forming layer on top of a colour-developing layer. The colour-forming layer contains microcapsules of defined compressive strength. When a sufficiently high pressure is applied, the microcapsules burst, creating a red coloured patch with colour intensity dependent on the local pressure. Prior to testing the CFRP specimens, the films were calibrated by compressing them between two flat platens at increments of pressure level, giving a calibrated pressure range of 35 MPa to 300 MPa. To ensure that a full pressure profile can

[1] Fujifilm Holdings Corporation, 7-3, Akasaka 9-chome, Minato-ku, Tokyo 107-0052, Japan

[2] One layer each of Fuji Prescale®. MS film, HS film, and HHS film.

be recorded, the CFRP specimens were unloaded before the pressure at the centre of the specimen attained a value of 250 MPa.

4 Results

4.1 Out-of-plane Compressive Response

Representative out-of-plane compressive responses (expressed in terms of average nominal pressure $\bar{p} \equiv -F / L^2$ versus nominal compressive strain $-\varepsilon_{zz}$) at a strain rate of $-\dot{\varepsilon}_{zz} = 8 \times 10^{-4} \text{s}^{-1}$ are presented in Fig. 2. The following observations are drawn from these results.

(i) The uncured laminate (A) deformed in a rate-dependent manner and, at an average value of pressure $\bar{p}_f$ and strain level of 20 - 25%, a limited load drop is observed for L = 5, 7, and 10 mm (as denoted by the symbol × in the figures). The smallest specimen (L = 3 mm) did not exhibit a load drop and underwent a large through thickness strain of up to 60% (at which point the test was terminated). The progressive increase in nominal pressure $\bar{p}$ with strain is due to the increase in area of the loaded cross-section. A pronounced size effect was present for material (A); this is consistent with the indirect tension mechanism and a large zone of shear lag at the periphery of the specimen. Attwood et al. (2014) have shown that the shear lag zone size scales inversely with matrix flow strength.

(ii) In broad terms, the magnitude of the specimen size effect decreases with increasing state of cure, see Fig. 2a to 2e. The nominal pressure at compressive failure $\bar{p}_f$ increases and the compressive strain at failure decreases with increasing state of cure. For example, focus attention on the choice L = 7 mm, see Fig. 2f: $\bar{p}_f$ increases from 175 MPa for material (A) to 1.2 GPa for material (E), and the corresponding strain level $-\varepsilon_{zz}$ drops from 25% for material (A) to 13% for material (E).

(iii) A concave-up (stiffening) $\bar{p}$ versus $-\varepsilon_{zz}$ initial response was observed for materials (A) to (C), see Fig. 2a to 2c and Fig. 2f. This stiffening response has been reported previously for the out-of-plane compression of unidirectional carbon fibre prepregs, see for example

Gutowski et al. (1987), Cai and Gutowski (1992), Gutowski and Dillon (1992), Hubert and Poursartip (2001). This stiffening response is caused by increased fibre packing at large compressive strains. For the fully cured state, material (E), failure intervenes before large compressive strains are achieved, and consequently a linear compressive response is obtained, see Fig. 2e.

4.2 Strain Rate Sensitivity

The nominal pressures at compressive failure $\bar{p}_f$ in the compression tests are summarised in Fig. 3a to 3e by plotting $\bar{p}_f$ versus specimen side length L at selected states of cure[1] and for 3 values of strain rate $-\dot{\varepsilon}_{zz}$. The strain rate sensitivity of $\bar{p}_f$ is the most pronounced for uncured material (A) and for partially cured material (B). Materials (C) to (E) possess higher states of cure and are almost rate insensitive. The above observations are consistent with the measurement of the out-of-plane longitudinal shear strength of the laminates at various shear strain rates, see Table 1.

The effect of matrix shear strength on the out-of-plane compressive strength is summarized in Fig. 3f for the choice L = 7 mm. Specifically, we plot $\bar{p}_f$ at the 3 selected values of strain rate versus the out-of-plane longitudinal shear strength τ_{OP}, as measured at a shear strain rate of $\dot{\gamma}_0 = 10^{-3}\text{s}^{-1}$, for materials (A) to (E). As the matrix shear strength τ_{OP} increases from 0.11 MPa to 99 MPa (from material (A) to (E)), the strain rate sensitivity of $\bar{p}_f$ decreases, while the magnitude of $\bar{p}_f$ increases by almost an order of magnidue.

4.3 Pressure Distribution of the Laminates during Compression

The pressure distributions on the top face of materials (A), (B), and (E) with L = 10 mm were measured by pressure sensitive film. For each material, about 10 tests were performed in order to obtain a relation between the peak pressure at the centre of the specimen $p_{\max}$ and the average pressure $\bar{p}$. This relation (not shown here for the sake of brevity) was used to identify,

[1] For small specimens of uncured material (A) where failure was not observed, data points were taken from the nominal pressure $\bar{p}$ when the compression tests were terminated at $-\varepsilon_{zz}$ = 60%.

for each material, the pressure level $\bar{p}$ for which $p_{\max}$ = 250 MPa. The pressure distribution for $p_{\max}$ = 250 MPa is given in Fig. 4 (a), (c), and (e) for materials (A), (B), and (E), respectively. Only 1/4 of each specimen in shown due to the symmetry of the specimen. The measured pressure profile $p(x)$ on materials (A), (B), (C), and (E) is plotted along the centre-line (y = 0) in Fig. 5 for selected values of $p_{\max}$ = 100 MPa, 200 MPa, and 250 MPa

Consider first Fig. 4. In the region near the periphery of the specimen, interlaminar shear occurs at the inter-layer between the alternating $0°$ and $90°$ plies. Within a shear lag zone (of length l_s) the pressure p builds up from the periphery towards the centre ($x = y = 0$), recall Fig. 1c. In the central region, within the peripheral shear lag zone, the pressure p remains uniform at a maximum value of $p_{\max}$. The width of the shear lag zone l_s decreases with increasing matrix shear strength, see Fig. 5.

4.4 Observed Deformation and Failure Mechanisms

First, consider the *deformation mechanism* of the compression specimens, as determined by terminating the tests on materials (A), (B) and (E) prior to the initial peak load on the load-displacement response. Specifically, repeat tests were performed on specimens of L = 7 mm and $-\dot{\varepsilon}_{zz} = 8\times10^{-4}\text{s}^{-1}$, and the tests were terminated at $-\varepsilon_{zz}$ = 12%; this strain level was selected by making use of the curves shown in Fig. 2f.

In order to observe the deformation state from one ply to the next, one side of the specimens was polished and gold coated prior to testing. Vertical lines of spacing ~ 0.5 mm were made using a scalpel blade to scratch (that is, remove) the coating. Post-test, the specimens were examined in a scanning electron microscope (SEM). SEM side-views of specimens compressed to $-\varepsilon_{zz}$ = 12% (before failure) revealed that the above makings changed from vertical lines to a 'square wave' pattern accompanied by ply extrusions at the specimen edges, as shown in Fig. 6a, 6c, and 6e. This pattern indicates intense shear at the inter-layer between the $0°$ and $90°$ plies near the periphery of the specimen, suggesting the presence of a shear lag zone. The magnitude of lateral deformation scales with the level of imposed compressive strain in the through thickness direction.

Second, consider the *failure mechanism*. It was difficult to observe fibre failure in the top view of each specimen, and so an additional set of observations was made post-failure on

specimens (A), (B), and (E). The failure strain is unambiguous for materials (B) and (E), whereas for material (A) it is assumed that failure occurs at a strain of $-\varepsilon_{zz} = 25\%$ immediately after the first load drop, see Fig. 2f. The failed specimens were held at $425\,^{\circ}\mathrm{C}$ for 90 minutes in air oven in order to pyrolyse the resin in the laminate, followed by de-plying using a scalpel blade (as detailed in Freeman (1982)). The specimens were observed in top view at mid-thickness using the SEM, see Fig. 6b, 6d, and 6f. Tensile fibre failure is apparent in all three materials. The sketch in Fig. 6g gives the interpretation of the images in Fig. 6a to 6f, and emphasises (i) the Poisson expansion of plies and (ii) ply tensile failure in a cross-ply laminate. The above observations are consistent with the indirect tension failure of Dyneema® cross-ply laminates under out-of-plane compression, see Attwood et al. (2014). We conclude that the CFRP cross-ply laminates (A) to (E) failed by the indirect tension mechanism.

5 Finite Element Analysis of the Out-of-plane Compressive Strength

5.1 Constitutive Law of Plies

Consider a unit cell comprising a $0°$ ply, an adjacent $90°$ ply, and an inter-layer between them, as illustrated in Fig. 7a. In order to specify the constitutive law for the inter-layer, we adopt the global co-ordinates (x, y, z) as shown in the figure. In specifying the constitutive law for the ply core, we limit our attention to the $90°$ ply such that ($x_1 \equiv x$, $x_2 \equiv y$, $x_3 \equiv z$). The constitutive laws for the inter-layer and ply core are closely related; therefore, we first give the behaviour of the inter-layer, and then specify the response of the ply core. For both the ply core and inter-layer, the total strain rate $\dot{\varepsilon}_{ij}^{tot}$ comprises an elastic contribution $\dot{\varepsilon}_{ij}^{el}$ and a rate-dependent contribution $\dot{\varepsilon}_{ij}^{pl}$, such that

$$\dot{\varepsilon}_{ij}^{tot} = \dot{\varepsilon}_{ij}^{el} + \dot{\varepsilon}_{ij}^{pl} \tag{2}$$

where subscripts *i* and *j* each range over (x, y, z), in the global coordinate system.

Consider first the inter-layer. The elastic response is taken to be isotropic with a modulus E and a Poisson's ratio ν, as given in Table 2. The modulus of the inter-layer is taken to equal the out-of-plane modulus E_3 of the core layer (i.e. $E \equiv E_3$), and the Poisson's

ratio of the inter-layer is taken the Poisson's ratio ν_{23} of the core layer (i.e. $\nu \equiv \nu_{23}$). The anisotropic non-associated, rate-dependent response is specified by

$$\dot{\varepsilon}_{ij}^{pl} \equiv \sum_{k=1}^{4} \dot{\lambda}^{(k)} \frac{\partial \Phi^{(k)}}{\partial \sigma_{ij}} \tag{3}$$

where $\Phi^{(k)}\left(\sigma_{ij}\right)$ is a set of four flow potentials and $\dot{\lambda}^{(k)}\left(\sigma_{ij}\right)$ is a set of four plastic multipliers. Assume that plastic straining is incompressible, but the magnitude of each component is pressure sensitive. The flow potentials $\Phi^{(k)}$ are taken as

$$\Phi^{(1)} \equiv \left|\sigma_{yy} - \sigma_{zz}\right| \tag{4a}$$

$$\Phi^{(2)} \equiv 2\left|\sigma_{xy}\right| \tag{4b}$$

$$\Phi^{(3)} \equiv 2\left|\sigma_{yz}\right| \tag{4c}$$

$$\Phi^{(4)} \equiv 2\left|\sigma_{xz}\right| \tag{4d}$$

and the plastic multipliers $\dot{\lambda}^{(k)}$ are specified by

$$\dot{\lambda}^{(k)} = \begin{cases} \dot{\varepsilon}_0^{(OP)} \left(\dfrac{\hat{\sigma}^{(k)}}{\sigma_0^{(OP)}} \right)^{1/m} & for\ \hat{\sigma}^{(k)} > 0 \\ 0 & for\ \hat{\sigma}^{(k)} \le 0 \end{cases}, k = 1,2,3,4 \tag{5}$$

in terms of $\hat{\sigma}^{(k)}$ where

$$\hat{\sigma}^{(k)} \equiv \Phi^{(k)} + 2\mu\sigma_h \tag{6}$$

Here, $\sigma_h \equiv \left(\sigma_{yy} + \sigma_{zz}\right)/2$ is the in-plane hydrostatic stress in the *y*-*z* plane and the coefficient μ represents the pressure dependency of the matrix. Note that the material parameters ($\dot{\varepsilon}_0^{(OP)}$ and $\sigma_0^{(OP)}$) of the inter-layer were measured by out-of-plane longitudinal shear tests, see Table 2.

Now limit attention to the $90°$ ply core such that ($x_1 \equiv x$, $x_2 \equiv y$, $x_3 \equiv z$). The elastic response is taken to be transversely isotropic along the x_1 axis (i.e. fibre direction), see Fig. 7c. The elastic constants in the local coordinates of the ply ($E_1, E_3, \nu_{31}, \nu_{23},$ and G_{12}) are listed in Table 2. The elastic properties of fully cured Hexply® 8552/IM7 (i.e. material (E)) were previously measured, whereas those of Materials (A) to (D) have not been measured but were deduced from the following arguments. The in-plane modulus E_1 is dominated by the fibres and therefore is set to equal the measurements for the fully cured material (E), see Table 2. For the out-of-plane modulus E_3, Figure 3 reveals that materials (A) to (D) have a concave-up (stiffening) response due to fibre compaction prior to failure at $-\varepsilon_{zz} > 13\%$. For the purpose of modelling the failure strength, we assume that the magnitude of E_3 for all materials is equal to the modulus in the compacted state, and approaches the transverse modulus of the fibre (i.e. 10 GPa for PAN-based carbon fibre, as reported by Ji et al. (2015)), see Table 2. Numerical experimentation, as well as a consideration of the analytical model, shows that $\bar{p}_f$ is insensitive to the magnitude of the moduli of the plies and of the inter-layers. Given that the focus of the study is on the sensitivity of $\bar{p}_f$ to the plastic properties of the matrix, predictions are only given for a fixed set of ply moduli, as given in Table 2.

The non-associated, rate-dependent response of the ply is also described by the above model with $\dot{\varepsilon}_0^{(OP)}$ and $\sigma_0^{(OP)}$ replaced by $\dot{\varepsilon}_0^{(IP)}$ and $\sigma_0^{(IP)}$, respectively, to represent in-plane shear, see Table 2. Furthermore, the plastic strain rates $\dot{\varepsilon}_{23}^{pl}$ and $\dot{\varepsilon}_{12}^{pl}$ are negligible compared to those in the inter-layers. Consequently, the flow potentials $\Phi^{(k)}$ for the ply are taken to be:

$$\Phi^{(1)} \equiv \left|\sigma_{22} - \sigma_{33}\right| \tag{7a}$$

$$\Phi^{(2)} \equiv 2\left|\sigma_{13}\right| \tag{7b}$$

$$\Phi^{(3)} \equiv 0 \tag{7c}$$

$$\Phi^{(4)} \equiv 0 \tag{7d}$$

such that $\dot{\varepsilon}_{23}^{pl} = \dot{\varepsilon}_{12}^{pl} = 0$ in the ply.

In the limit $m \to 0$ the above constitutive model reduces to a rate-independent, non-associated description. For example, (3), (5) and (7a) are combined to provide the yield criterion:

$$\left|\sigma_{22} - \sigma_{33}\right| + \mu\left(\sigma_{22} + \sigma_{33}\right) - 2\tau_y = 0 \tag{8}$$

where τ_y is the value of $\left|\sigma_{33}\right|$ for the case $\sigma_{22} = -\sigma_{33}$ (corresponding to a state of pure shear in the (x_2, x_3) plane; hence the notation for τ_y). The strain rate sensitivity of materials (A) to (E) were measured by $\pm 45°$ tensile tests and short beam tests (see Appendix A) and their sensitivity coefficients m are reported in Table 2. Note that materials (C) to (E) are almost rate insensitive, thus m is taken to equal zero.

Multiple research groups have conducted out-of-plane compression tests on UD plies of carbon fibre/epoxy and glass fibre/epoxy composites with superimposed hydrostatic pressure and have observed pressure dependency as given by (8), see for example Hine et al. (1999, 2005), Pae and Rhee (1995), and Parry and Wronski (1990). In these studies, unidirectional (UD) plies were first loaded to a constant hydrostatic pressure *P* in a triaxial pressure cell. The UD plies were then compressed in the x_3-direction, transverse to the fibre-direction, as illustrated in Fig. 8a. The stress state is of the form $\sigma_{11} = \sigma_{22} = -P$ and $\sigma_{33} = -P + \sigma_a$, where σ_a is the applied compressive stress. These researchers found that both the compressive yield strength and the failure strength increase proportionally with the superimposed hydrostatic pressure P. Fig. 8a presents these data in terms of the normalised stress components σ_{22}/τ_y and σ_{33}/τ_y at yield; here, the yield point is taken to coincide with the 0.2% offset strength in the σ_{33} versus ε_{33} stress-strain response. A comparison with (8) reveals that fully cured carbon fibre/epoxy has a coefficient of $\mu = 0.2$. Preliminary FE simulations also showed that $\mu = 0.2$ is appropriate for the compressive yield strength of materials (B) to (E), thus we set $\mu = 0.2$ for materials (B) to (E) in the FE model, see Table 2. Preliminary FE simulations also showed that the choice $\mu = 0.05$ is appropriate for the compressive yield strength of uncured material (A), see Table 2. Such a low value of μ has

also been reported for Dyneema® plies that consist of thermoplastic polyurethane matrix, see Attwood et al. (2014).

5.2 Failure Criterion for each Composite Ply

As mentioned in Section 1.2, the tensile strength of dry carbon fibre tows and carbon fibre/epoxy plies decreases with increasing superimposed hydrostatic pressure, see Hine et al. (1999, 2005), Parry and Wronski (1985, 1986), Sigley et al. (1991), and Zinoviev and Tsvetkov (1998). To account for the pressure dependence of fibre tensile strength, we propose the following tensile failure criterion for the carbon fibre UD plies of the current study:

$$\sigma_{11} < S_L^+ + \frac{\alpha}{2}\left(\sigma_{22} + \sigma_{33}\right) \tag{9}$$

where S_L^+ is the ply tensile strength at $\sigma_h \equiv \left(\sigma_{22} + \sigma_{33}\right)/2$ equal to zero (i.e. the uniaxial tensile strength of a UD ply), and the coefficient α quantifies the pressure-dependence of the tensile strength. This coefficient should not be confused with the pressure coefficient μ for the matrix flow strength. When $\alpha = 0$, the above tensile failure criterion reduces to the criterion ($\sigma_{11} < S_L^+$) as used by Attwood et al. (2014). The available data from the literature suggests that $\alpha \sim 2$ for the cured CFRP plies in the current system, as demonstrated below.

In-plane tensile tests on UD plies of carbon fibre/epoxy, glass fibre/epoxy, and Kevlar® composites with superimposed hydrostatic pressure have already been reported in the literature. For example, see Parry and Wronski (1985) and Hine et al. (1999) for data on carbon fibre/epoxy composites; Parry and Wronski (1986), Sigley et al. (1991), and Hine et al. (2005) for data on glass fibre/epoxy composites; and Zinoviev and Tsvetkov (1998) on Kevlar® composites. In general, the in-plane tensile strength of UD plies in these composites decreases with increasing superimposed pressure. In these studies, the UD plies were first loaded to a constant hydrostatic pressure with a magnitude P in a triaxial pressure cell, followed by tensile loading in the x_1-direction parallel to the fibre. The stress state at ply tensile failure was $\sigma_{22} = \sigma_{33} = -P$ and $\sigma_{11} = -P + \sigma_a$, where σ_a is the applied tensile stress. Fig. 8b presents these data in terms of the normalised stress components σ_{11}/S_L^+ and $\sigma_{22}/S_L^+ = \sigma_{33}/S_L^+$ at

ply tensile failure. Upon fitting (9) to these data we find that α ranges from ~ 1 to ~ 2 in the different composite systems, with $\alpha \sim 2$ for CFRP composites. Consequently, the current FE model assumes that $\alpha = 2$ in all the studied CFRP plies and S_L^+ is taken from the datasheet of Hexcel Composites (2013), see Table 2.

5.3 Finite Element Method

The finite element (FE) method was used to simulate the out-of-plane compressive response of the cross-ply laminate with a specimen side length $L \times L$ consisting of a stack of alternating $0°$ and $90°$ plies. We shall assume that the stack contains a sufficiently large number of plies that the response is adequately modelled by a unit cell comprising a pair of $0°$ and $90°$ plies, and symmetry allows us to analyse only a quarter section of the in-plane dimension $L/2 \times L/2$. The global Cartesian directions *x* and *y* are in-plane and orthogonal, lie parallel to the edges of the laminate, while *z* represents the out-of-plane loading direction, see Fig. 7a. Periodic boundary conditions are enforced at the top and bottom surfaces in the stack of $0°$ and $90°$ plies. The displacements of boundaries satisfy:

$$u_x^{(A)} = u_x^{(B)} \tag{10a}$$

$$u_y^{(A)} = u_y^{(B)} \tag{10b}$$

$$u_z^{(A)} = u_z^{(B)} - 2\left(H + 2h\right)\varepsilon_{zz}^{\infty} \tag{10c}$$

where $\left(H + 2h\right)$ represents the ply thickness, the superscripts (A) and (B) refer to the top and bottom surfaces of the stack, respectively, and $\varepsilon_{zz}^{\infty}$ is the macroscopic strain imposed on the unit cell. Quarter symmetry is enforced along the centre-lines, see Fig. 7b, and displacement continuity is assumed along the inter-layer between the two plies. The overall lateral spread of the cross-ply specimen is uniform in the through-thickness direction, and this is due to the ply-by-ply constraint rather than due to tooling constraint, see Fig. 6. Hence, it is adequate to analyse a representative unit cell rather than the full thickness of the specimen between the loading platens.

Finite element simulations were performed using a dynamic implicit version of the commercial FE package ABAQUS (version 6.12), and the constitutive laws of each ply were implemented as a user material subroutine (UMAT). The dynamic implicit version was selected in order to increase the simulation efficiency by relaxing the constraint on the calculation of

the stiffness matrix. To ensure that the quasi-static equilibrium response was achieved, the ratio of kinetic energy to total energy was monitored and ensured to be less than 0.1%.

Now consider the construction of each ply, see Fig. 7c. The material coordinate system of each unidirectional (UD) ply is defined such that the x_1-direction is parallel to the fibres, the x_2-direction is the in-plane direction transverse to the fibre, and the x_3-direction is the out-of-plane direction of the ply (and parallel to *z*-direction in the global coordinate system). Each ply, of height H, is sandwiched between two inter-layers of height $h \equiv H/129$, see Table 1. The physical motivation for the inter-layer is the observed presence of a thin resin rich region between neighbouring plies that allows for intense plastic shear, whereas plastic shear in inhibited within each ply by the presence of fibres. Both the core and inter-layers were discretised using eight-noded linear brick elements with reduced integration (C3D8R in the ABAQUS notation). Each of these layers comprised 22,500 cuboidal elements.

5.4 Predictions

The predicted compressive response (in terms of average pressure $\bar{p} \equiv -F/L^2$ versus compressive strain $-\varepsilon_{zz}$) is compared with the measurements in Fig. 9. Since the FE simulations consider deformation at the ply level, they do not capture the initial stiffening response that is caused by fibre packing at the sub-ply level. As the state of cure of the laminates increases, the stiffening response becomes less pronounced; indeed, it is no longer detectable for material (E). As a result, for material (E), both the failure pressure and failure strain as calculated from the FE simulations are in good agreement with the measurements. Despite this feature of initial stiffening in the observed response, the FE simulations adequately predict the average pressure at failure $\bar{p}_f$ as a function of matrix strength (as dictated by degree of cure) and of specimen dimension *L*.

The pressure distributions as calculated from the FE simulations are compared with the pressure sensitive film measurements at $p_{\max}$ = 250 MPa, see Fig. 4. Recall that $p_{\max}$ is defined to be the maximum pressure at the centre ($x = y = 0$) of the specimen on the *x*-*y* plane. The FE simulations are in support of the measured pressure profiles, and confirm that the size effect is associated with the existence of a shear lag at the periphery of the specimens. Both the FE simulations and the experiments showed that p is at a minimum along the periphery

of the specimens and builds up towards the centre of the specimens, see Fig. 5. The length of the shear lag zone l_s as calculated from the FE simulations are in good agreement with the measurements. Furthermore, the FE simulations capture the decrease in shear lag length l_s with increasing state of matrix cure from material (A) to material (E).

The predicted dependence of $\overline{p}_f$ upon specimen side length L is included in Fig. 3 for selected values of compressive strain rate $-\dot{\varepsilon}_{zz}$. The FE simulations give the same pronounced size effect, and also predict the same degree of strain rate sensitivity as that observed for each state of cure. Furthermore, the FE method captures the sensitivity of mean failure pressure $\overline{p}_f$ to matrix shear strength as parameterized by τ_{OP} for specimens of size L = 7 mm, see Fig. 3f. It is striking that $\overline{p}_f$ increases by almost an order of magnitude with increasing state of matrix cure.

Additional insight is now derived by the development of an analytical model for the out-of-plane compressive response of the cross-ply laminate, based on the main features of the FE solution. The model reveals the sensitivity of $\overline{p}_f$ and shear lag length l_s to specimen side length L and out-of-plane strain rate $\dot{\varepsilon}_{33}^{tot}$.

6 An analytical model for the out-of-plane compressive strength

First, consider the deformation state within the shear lag zone, near the periphery of the specimen, and limit attention to the $90°$ ply with ($x_1 \equiv x$, $x_2 \equiv y$, $x_3 \equiv z$), see Fig. 1c. Using the local coordinates of the $90°$ ply, the plastic shear strain rate $\dot{\varepsilon}_{23}^{pl}$ of the inter-layer is expressed by substituting (4) and (5) into (3), to give

$$\dot{\varepsilon}_{23}^{pl} = \dot{\varepsilon}_0^{(OP)} \left(\frac{\hat{\sigma}_{OP}^{(3)}}{\sigma_0^{(OP)}} \right)^{1/m} \tag{11}$$

where $\hat{\sigma}_{OP}^{(3)} = 2\sigma_{23} + \mu\sigma_{22} + \mu\sigma_{33}$, $\sigma_{33} \le 0$ and $|\sigma_{33}| > |\sigma_{22}|$. Throughout, the subscript (OP) and superscript (OP) denote out-of-plane longitudinal shear. Similarly, using the local co-

ordinates of the $90°$ ply, the plastic normal strain rate $\dot{\varepsilon}_{33}^{pl}$ of the core layer can be expressed by substituting (7) and (5) into (3), to give

$$\dot{\varepsilon}_{33}^{pl} = \dot{\varepsilon}_0^{(IP)} \left(\frac{\hat{\sigma}_{IP}^{(1)}}{\sigma_0^{(IP)}} \right)^{1/m} \tag{12}$$

where $\hat{\sigma}_{IP}^{(1)} = \sigma_{22}(\mu+1) + \sigma_{33}(\mu-1)$, $\sigma_{33} \le 0$ and $|\sigma_{33}| > |\sigma_{22}|$. The subscript (IP) and superscript (IP) both denote the ply core layer.

The relationship between the out-of-plane shear stress σ_{23} and the in-plane normal stress σ_{22} within the shear lag zone can be expressed by elimination of σ_{33} from (11) and (12), to give

$$\sigma_{23} = \frac{1}{2}\sigma_0^{(OP)} \left(\frac{\left|\dot{\varepsilon}_{23}^{pl}\right|}{\dot{\varepsilon}_0^{(OP)}} \right)^m + \frac{1}{2}\hat{\mu}\sigma_0^{(IP)} \left(\frac{\left|\dot{\varepsilon}_{33}^{pl}\right|}{\dot{\varepsilon}_0^{(IP)}} \right)^m - \hat{\mu}\sigma_{22} \tag{13}$$

where $\hat{\mu} \equiv \mu/(1-\mu)$. Overall force equilibrium in the x_2-direction of a $90°$ ply (with the origin of the local coordinate system located at the periphery of the specimen, as shown in Fig 1c) dictates that:

$$H\frac{d\sigma_{22}}{dx_2} = -2\sigma_{23} \tag{14}$$

The in-plane normal stress $\sigma_{22}(x_2)$ can be determined by substituting for σ_{23} from (13). However, this expression does not have an explicit solution and can only be solved numerically. The accurate solution was obtained from the FE simulation, but an approximate analytical solution can be obtained by assuming that the material is under large deformation and that the elastic strain rate is negligible compared to the plastic strain rate, i.e. $\dot{\varepsilon}_{23}^{pl} \approx \dot{\varepsilon}_{23}^{tot}$ and $\dot{\varepsilon}_{33}^{pl} \approx \dot{\varepsilon}_{33}^{tot}$. We further assume a uniform shear strain rate over the shear lag zone l_s such that $\dot{\varepsilon}_{23}^{tot}$ in the inter-layer can be estimated in terms of the applied out-of-plane strain rate $\dot{\varepsilon}_{33}^{tot}$ when considering incompressibility in the $x_2 - x_3$ plane (i.e. $\dot{\varepsilon}_{22}^{tot} = -\dot{\varepsilon}_{33}^{tot}$):

$$\dot{\varepsilon}_{23}^{tot} = \frac{d\dot{u}_2}{2dx_3} \approx \frac{\dot{\varepsilon}_{22}^{tot} l_s}{2h} \approx \frac{-\dot{\varepsilon}_{33}^{tot} l_s}{2h} \tag{15}$$

where $\dot{u}_2$ is the displacement rate in the x_2-direction and h is the height of the inter-layer. Now substitute for $\dot{\varepsilon}_{23}^{tot}$ and $\dot{\varepsilon}_{33}^{tot}$ into (13) and make use of (14) to obtain

$$-H\frac{d\sigma_{22}}{dx_2} = \sigma_0^{(OP)}\left(\frac{\left|\dot{\varepsilon}_{33}^{tot}\right| l_s}{2\dot{\varepsilon}_0^{(OP)} h}\right)^m + \hat{\mu}\sigma_0^{(IP)}\left(\frac{\left|\dot{\varepsilon}_{33}^{tot}\right|}{\dot{\varepsilon}_0^{(IP)}}\right)^m - 2\hat{\mu}\sigma_{22} \tag{16}$$

The above expression can be integrated to determine the in-plane normal stress $\sigma_{22}(x_2)$ and $\sigma_{11}(x_2)$ to give

$$\sigma_{11} = -\sigma_{22} = \left[\frac{\sigma_0^{(OP)}}{2\hat{\mu}}\left(\frac{\left|\dot{\varepsilon}_{33}^{tot}\right| l_s}{2\dot{\varepsilon}_0^{(OP)} h}\right)^m + \frac{\sigma_0^{(IP)}}{2}\left(\frac{\left|\dot{\varepsilon}_{33}^{tot}\right|}{\dot{\varepsilon}_0^{(IP)}}\right)^m\right]\left[\exp\left(\frac{2\hat{\mu}x_2}{H}\right) - 1\right] \tag{17}$$

This expression shows that ply tensile stress in the fibre direction σ_{11} rises exponentially from the periphery ($x_2 = 0$) towards the centre of the specimen. We define the size of the shear lag zone l_s to be distance from the periphery to the location where $\sigma_{11}(x_2)$ reaches a value of $\sigma_{11}^{\max}$. Thus, l_s can be determined by substituting for $x_2 = l_s$ and $\sigma_{11} = \sigma_{11}^{\max}$ into (17):

$$l_s = \frac{H}{2\hat{\mu}}\ln\left\{1 + \sigma_{11}^{\max}\left[\frac{\sigma_0^{(OP)}}{2\hat{\mu}}\left(\frac{\left|\dot{\varepsilon}_{33}^{tot}\right| l_s}{2\dot{\varepsilon}_0^{(OP)} h}\right)^m + \frac{\sigma_0^{(IP)}}{2}\left(\frac{\left|\dot{\varepsilon}_{33}^{tot}\right|}{\dot{\varepsilon}_0^{(IP)}}\right)^m\right]^{-1}\right\} \tag{18}$$

This is an implicit expression for l_s but nonetheless direct examination reveals that l_s decreases with increasing $\left|\dot{\varepsilon}_{33}^{tot}\right|$ and with increasing creep strength $\sigma_0^{(OP)}$ and $\sigma_0^{(IP)}$, that is with increasing matrix cure. The corresponding out-of-plane pressure $p(x_2) \equiv -\sigma_{33}(x_2)$ within the shear lag zone can be obtained by substituting for $\sigma_{11} = -\sigma_{22}$ from (18) into (17) to give:

$$p = \left[\frac{\sigma_0^{(OP)}}{2} \left(\frac{1+\mu}{\mu} \right) \left(\frac{\left| \dot{\varepsilon}_{33}^{tot} \right| l_s}{2\dot{\varepsilon}_0^{(OP)} h} \right)^m + \frac{\sigma_0^{(IP)}}{2} \left(\frac{1+\mu}{1-\mu} \right) \left(\frac{\left| \dot{\varepsilon}_{33}^{tot} \right|}{\dot{\varepsilon}_0^{(IP)}} \right)^m \right] \left[\exp\left(\frac{2\hat{\mu} x_2}{H} \right) - 1 \right] + \frac{\sigma_0^{(IP)}}{1-\mu} \left(\frac{\left| \dot{\varepsilon}_{33}^{tot} \right|}{\dot{\varepsilon}_0^{(IP)}} \right)^m$$

for $\left(x_2 \le l_s \right)$ (19)

6.2 Pressure Distribution in the Central Region of the Specimen

In the central region $\left(x_2 > l_s \right)$ the pressure p remains uniform at a maximum value of $p_{\max}$. This maximum pressure $p_{\max}$ is governed by the elastic, rate dependent plastic flow, which can be determined by substituting $p_{\max} = \sigma_{33}$ and $\sigma_{22} = -\sigma_{11}$ into (12):

$$p_{\max} = \left(\frac{1+\mu}{1-\mu} \right) \sigma_{11}^{\max} + \frac{\sigma_0^{(IP)}}{1-\mu} \left(\frac{\left| \dot{\varepsilon}_{33}^{tot} \right|}{\dot{\varepsilon}_0^{(IP)}} \right)^m \quad \text{for} \quad \left(x_s > l_s \right) \tag{20}$$

where $\sigma_{11}^{\max}$ is the ply tensile stress in the fibre direction σ_{11} in the central region. As the out-of-plane compression test proceeds, $\sigma_{11}^{\max}$ and $p_{\max}$ at the centre of the specimen increase in magnitude. Indirect tension failure occurs when the stress state in the centre of specimen reaches the ply tensile failure criterion in (9). Thus, $\sigma_{11}^{\max}$ at failure can be expressed as:

$$\sigma_{11}^{\max} = \frac{2S_L^+ - \alpha p_{\max}}{2+\alpha} \tag{21}$$

The maximum pressure $p_{\max}$ at indirect tension failure p_f can be determined by substituting $\sigma_{11}^{\max}$ from (21) into (20):

$$p_f = \frac{\left(\frac{2+\alpha}{2} \right) \sigma_0^{(IP)} \left(\left| \dot{\varepsilon}_{33}^{tot} \right| / \dot{\varepsilon}_0^{(IP)} \right)^m + (1+\mu) S_L^+}{1-\mu+\alpha} \tag{22}$$

Similarly, the maximum in-plane tensile stress $\sigma_{11}^{\max}$ at indirect tension failure σ_{11}^f can be expressed by substituting $\sigma_{11}^{\max}$ from (21) into (22):

$$\sigma_{11}^{f} = \frac{\left(\frac{2+\alpha}{2}\right)\sigma_0^{(IP)}\left(\left|\dot{\varepsilon}_{33}^{tot}\right| / \dot{\varepsilon}_0^{(IP)}\right)^m + \left(2-2\mu+\alpha-\alpha\mu\right)S_L^+}{\left(2+\alpha\right)\left(1-\mu+\alpha\right)} \tag{23}$$

The shear lag length associated with the indirect tension failure l_s^f can be determined by substituting σ_{11}^f into (18):

$$l_s^f = \frac{H\left(1-\mu\right)}{2\mu}\ln\left\{1+\sigma_{11}^f\left[\frac{\sigma_0^{(OP)}}{2}\left(\frac{1-\mu}{\mu}\right)\left(\frac{\left|\dot{\varepsilon}_{33}^{tot}\right| l_s^f}{2\dot{\varepsilon}_0^{(OP)}h}\right)^m + \frac{\sigma_0^{(IP)}}{2}\left(\frac{\left|\dot{\varepsilon}_{33}^{tot}\right|}{\dot{\varepsilon}_0^{(IP)}}\right)^m\right]^{-1}\right\} \tag{24}$$

We conclude from (22) and (23) that the failure pressure p_f and in-plane tensile stress σ_{11}^f both increases with $\sigma_0^{(IP)}\left(\left|\dot{\varepsilon}_{33}^{tot}\right| / \dot{\varepsilon}_0^{(IP)}\right)^m$, thereby revealing the explicit dependence upon the creep response of the matrix. We emphasise that (22) and (24) show that a higher out-of-plane strain rate $\dot{\varepsilon}_{33}^{tot}$ results in an increase in p_f and a decrease in l_s^f. Equations (22) and (24) also suggest that both p_f and l_s^f are independent of the specimen side length L. For a given state of cure and applied strain rate $\dot{\varepsilon}_{33}^{tot}$, the maximum pressure p_f and the shear lag length l_s^f would remain unchanged as the specimen side length L increases. However, as L increases, the proportion of the specimen that consists of the shear lag zone (with length l_s^f) would decrease, and consequently $\bar{p}_f$ increases. The calculation of $\bar{p}_f$ is now detailed.

6.3 Calculation of Average Failure Pressure

The compressive load F on the specimen can be determined by integrating the local pressure p over the cross-section:

$$F = 4\int_0^{L/2}\int_0^{L/2} p\,dx_2\,dx_1 \quad \text{for} \quad \left(L/2 < l_s^f\right) \text{ and} \tag{25a}$$

$$F = 4\int_0^{l_s^f}\int_0^{l_s^f} p\,dx_2 dx_1 + 4\left(L - 2l_s^f\right)\int_0^{l_s^f} p\,dx_2 + p_f\left(L - 2l_s^f\right)^2 \quad \text{for} \quad \left(L/2 \geq l_s^f\right) \qquad (25b)$$

The average pressure at failure $\bar{p}_f$ is defined by $\bar{p}_f \equiv F / L^2$. The above analytical model provides some insight into the effect of applied strain rate $\dot{\varepsilon}_{33}^{tot}$ and specimen side length L on $\bar{p}_f$. A comparison of the analytic predictions for $\bar{p}_f$, as based on (25a,b), with the measured response and the finite element predictions is given in Fig. 3. In broad terms, the analytical model is able to capture the sensitivity of $\bar{p}_f$ to the specimen size, to the applied strain rate, and to the degree of matrix cure. The size effect is most pronounced when the specimen size is on the order of the shear lag dimension l_s^f as given by (24); it is evident from Fig. 3 that the analytical model correctly predicts that l_s^f decreases with increasing strain rate and with increasing matrix cure.

8 Concluding Remarks

Our study has revealed that indirect tension is the active failure mechanisms of CFRP $[0°/90°]_8$ cross-ply laminates under quasi-static uniaxial out-of-plane compression, for a wide range of matrix cure. The matrix shear strength increases from 0.1 MPa to 100 MPa with the degree of cure. Out-of-plane compression tests were conducted on the above laminates with various specimen side lengths L and at various applied strain rates. Under compression, each ply expanded in the direction transverse to the fibre, stretching the adjacent plies in the fibre direction and causing fibre tensile failure. There was one observed exception to this behaviour, as follows. Laminates with the lowest state of cure (i.e. uncured prepregs) and small specimen size ($L < 5$ mm) that were tested at a low applied strain rate ($-\dot{\varepsilon}_{zz} = 8\times10^{-4}\text{s}^{-1}$) did not display a load drop and underwent large through thickness strain of up to 60% (at which point the test was terminated). The level of imposed pressure at the centre of this specimen was insufficient to lead to fibre fracture by indirect tension.

The sensitivity of compressive strength to specimen size and to applied strain rate have also been assessed. The compressive strength increases with increasing applied strain rate due

to the rate-dependent response of the matrix in the uncured and partially cured state. The compressive strength increases with increasing specimen size, and this is due to the presence of a shear lag zone at the periphery of the specimen.

Contact pressure measurements revealed that, during compression, pressure builds up from the periphery towards the centre of specimen, indicative of a shear lag zone. The size of the shear lag zone decreased as the matrix shear strength increased and eventually became a negligible proportion of the entire specimen. Thus, for autoclaved fully cured laminates, the compressive strength was insensitive to specimen size. Tool friction has a minor effect on the out-of-plane compressive strength by the following argument. Lubrication of the platens was used in all compression tests. It is emphasised that lateral constraint is imposed from one ply to the next of the cross-ply specimen, and so the presence or absence of tool friction will have a negligible influence on the magnitude of $\overline{p}_f$. This behaviour is in marked contrast to the out-of-plane compressive strength of a unidirectional specimen.

Finite element (FE) simulations and analytical models have been developed to predict the out-of-plane compressive strength of the cross-ply laminates. The models reveal that the pressure increases from the periphery of the specimen towards the centre in a shear lag manner. In the central region, surrounded by the peripheral shear lag zone, the pressure remains uniform at a maximum value. Furthermore, the models indicate that an increase in matrix shear strength raises the pressure required to cause indirect tension failure and decreases the size of the shear lag zone at failure, which has the combined effect of increasing the compressive strength. The average compressive strength also rises with increasing specimen size, as this reduces the proportion of the specimen that consists of the shear lag zone. Overall, both the FE simulations and the analytical predictions are in excellent alignment with the experimental data.

The above description of the indirect tension mechanism is consistent with the findings from Attwood et al. (2014), who observed this mechanism through compression tests on Dyneema® cross-ply laminates. O'Masta et al. (2015) have more recently revealed that Dyneema® cross-ply plates also fail by indirect tension under ballistic loading. Likewise, Yu et al. (Yu *et al.*, 2017) have demonstrated that the indirect tension mechanism is active in the ballistic penetration of CFRP cross-ply beams.

Acknowledgements

The research work was sponsored by the Office of Naval Research (ONR), U.S. (Prime Award No. N62909-14-1-N232). The raw composite materials and the autoclave manufacturing process were generously provided by Hexcel Ltd. Finally, the studentship of B. Yu was sponsored by the Croucher Foundation.

REFERENCES

Argon, A. S., Andrews, R. D., Godrick, J. A. and Whitney, W. (1968) 'Plastic deformation bands in glassy polystyrene', *Journal of Applied Physics*, 39(3), pp. 1899–1906.

Attwood, J. P., Khaderi, S. N., Karthikeyan, K., Fleck, N. A., Omasta, M. R., Wadley, H. N. G. and Deshpande, V. S. (2014) 'The out-of-plane compressive response of Dyneema® composites', *Journal of the Mechanics and Physics of Solids*. Elsevier, 70(1), pp. 200–226.

Attwood, J. P., Russell, B. P., Wadley, H. N. G. and Deshpande, V. S. (2016) 'Mechanisms of the penetration of ultra-high molecular weight polyethylene composite beams', *International Journal of Impact Engineering*. Elsevier Ltd, 93, pp. 153–165.

Cai, Z. and Gutowski, T. (1992) 'The 3-D Deformation Behavior of a Lubricated Fiber Bundle', *Journal of Composite Materials*, 26(8), pp. 1207–1237.

Collings, T. A. (1974) 'Transverse compressive behaviour of unidirectional carbon fibre reinforced plastics', *Composites*, 5(3), pp. 108–116.

Daniel, I. M., LaBedz, R. H. and Liber, T. (1981) 'New method for testing composites at very high strain rates', *Experimental Mechanics*, 21(2), pp. 71–77.

Freeman, S. M. (1982) 'Characterization of lamina and interlaminar damage in graphite/epoxy composites by the deply technique', in Daniel, I. (ed.) *Composite Materials: Testing and Design (6th Conference), STP28473S*. West Conshohocken, PA, pp. 50–62.

Gates, T. S. and Sun, C. T. (1991) 'Elastic/viscoplastic Constitutive Model for Fiber Reinforced Thermoplastic Composites', *AIAA Journal*, 29(3), pp. 457–463.

González, C. and LLorca, J. (2007) 'Mechanical behavior of unidirectional fiber-reinforced polymers under transverse compression: Microscopic mechanisms and modeling', *Composites Science and Technology*, 67(13), pp. 2795–2806.

Gutowski, T. G., Cai, Z., Bauer, S., Boucher, D., Kingery, J. and Wineman, S. (1987) 'Consolidation Experiments for Laminate Composites', *Journal of Composite Materials*, 21(July), pp. 650–669.

Gutowski, T. G. and Dillon, G. (1992) 'The Elastic Deformation of Lubricated Carbon Fiber Bundles: Comparison of Theory and Experiments', *Journal of Composite Materials*, 26(16), pp. 2330–2347.

Hexcel Composites (2013) *HexPly® 8552 epoxy matrix (180°C/356F curing matrix), product data, Publication FTA 072e.*

Hine, P. J., Duckett, R. A., Kaddour, A. S., Hinton, M. J. and Wells, G. M. (2005) 'The effect of hydrostatic pressure on the mechanical properties of glass fibre/epoxy unidirectional composites', *Composites Part A: Applied Science and Manufacturing*, 36(2 SPEC. ISS.), pp. 279–289.

Hine, P. J., Duckett, R. A., van Schepdael, L. J. J. M., Hamoen, J. R., van den Oever, M. J. A. and van den Berg, R. W. (1999) 'The effect of high pressure on the failure of unidirectional carbon fibre/epoxy composites', in Hogg, P. (ed.) *5th conference on deformaiton and fracture of composites*. London, pp. 251–259.

Hubert, P. and Poursartip, A. (2001) 'Method for the direct measurement of the fibre bed compaction curve of composite prepregs', *Composites Part A: Applied Science and Manufacturing*, 32(2), pp. 179–187.

Ji, X., Wang, C., Francis, B. A. P., Chia, E. S. M., Zheng, L., Yang, J., Joshi, S. C. and Chen, Z. (2015) 'Mechanical and Interfacial Properties Characterisation of Single Carbon Fibres for Composite Applications', *Experimental Mechanics*, 55(6), pp. 1057–1065.

Karthikeyan, K., Russell, B. P., Fleck, N. A., Wadley, H. N. G. and Deshpande, V. S. (2013) 'The effect of shear strength on the ballistic response of laminated composite plates', *European Journal of Mechanics, A/Solids*. Elsevier Masson SAS, 42, pp. 35–53.

Leigh Phoenix, S. and Porwal, P. K. (2003) 'A new membrane model for the ballistic impact response and V50 performance of multi-ply fibrous systems', *International Journal of Solids and Structures*, 40(24), pp. 6723–6765.

Marlett, K. (2011) *Hexcel 8552 IM7 Unidirectional Prepreg 190 gsm & 35%RC Qualification Material Property Data Report*.

O'Masta, M. R., Crayton, D. H., Deshpande, V. S. and Wadley, H. N. G. (2015) 'Mechanisms of penetration in polyethylene reinforced cross-ply laminates', *International Journal of Impact Engineering*. Elsevier Ltd, 86, pp. 249–264.

Pae, K. D. and Rhee, K. Y. (1995) 'Effects of hydrostatic pressure on the compressive behavior of thick laminated 45o and 90o unidirectional graphite-fiber/epoxy-matrix composites',

Composites Science and Technology, 53(3), pp. 281–287.

Parry, T. V. and Wronski, A. S. (1985) 'The effect of hydrostatic pressure on the tensile properties of pultruded CFRP', *Journal of Materials Science*, 20(6), pp. 2141–2147.

Parry, T. V. and Wronski, A. S. (1986) 'The tensile properties of pultruded GRP tested under superposed hydrostatic pressure', *Journal of Materials Science*, 21(12), pp. 4451–4455.

Parry, T. V. and Wronski, A. S. (1990) 'The effect of hydrostatic pressure on transverse strength of glass and carbon fibre-epoxy composites', *Journal of Materials Science*, 25(7), pp. 3162–3166. doi: 10.1007/BF00587668.

Rabinowitz, S., Ward, I. M. and Parry, J. S. C. (1970) 'The effect of hydrostatic pressure on the shear yield behaviour of polymers', *Journal of Materials Science*, 5(1), pp. 29–39.

Sigley, R. H., Wronski, A. S. and Parry, T. V. (1991) 'Tensile failure of pultruded glass-polyester composites under superimposed hydrostatic pressure', *Composites Science and Technology*, 41(4), pp. 395–409.

Slaughter, W. S., Budiansky, B. and Fleck, N. A. (1993) 'Compressive Failure of Fiber Composites: The Roles of Multiaxial Loading and Creep', *Journal of Engineering Materials and Technology*, 115(3), pp. 308–313.

Soutis, C. and Turkmen, D. (1997) 'Moisture and temperature effects of the compressive failure of CFRP unidirectional laminates', *Journal of Composite Materials*, 31(8), pp. 832–849.

Staab, G. H. and Gilat, A. (1995) 'High strain rate response of angle-ply glass/epoxy laminates', *Journal of Composite Materials*, 29(10), pp. 1308–1320.

Sun, C. T. and Chen, J. L. (1989) 'A Simple Flow Rule for Characterizing Nonlinear Behavior of Fiber Composites', *Journal of Composite Materials*, 23(10), pp. 1009–1020.

Ward, I. M. (1971) 'Review: The yield behaviour of polymers', *Journal of Materials Science*, 6(11), pp. 1397–1417.

Weeks, C. A. and Sun, C. T. (1998) 'Modeling non-linear viscoplastic behavior in fiber-reinforced composites', *Composites Science and Technology*, 3538(97), pp. 603–611.

Woodward, R. L., Egglestone, G. T., Baxter, B. J. and Challis, K. (1994) 'Resistance to penetration and compression of fibre-reinforced composite materials', *Composites*

Engineering, 4(3). doi: 10.1016/0961-9526(94)90083-3.

Yu, B., Karthikeyan, K., Deshpande, V. S. and Fleck, N. A. (2017) 'Perforation resistance of CFRP beams to quasi-static and ballistic loading: The role of matrix strength', *International Journal of Impact Engineering*, 108, pp. 389–401.

Zinoviev, P. A. and Tsvetkov, S. V (1998) 'Organic-Fiber-Reinforced Plastics Under Hydrostatic Pressure', 3538(97).

Appendix A

The matrix shear strength of the laminates in 5 states of cure was measured using two shear test methods (following the recommendations in ASTM standard D3518 and D2344). A $\pm 45°$ tensile test was used to measure the in-plane shear strength and a short beam shear test was used to measure the longitudinal, out-of-plane interlaminar shear strength of the laminates at various shear strain rates.

A.1 In-plane $\pm 45°$ Tensile Test

Dog-bone tensile specimens of $[\pm 45°]_{4s}$ lay-up, thickness t = 2 mm (16 plies), and width w = 10 mm within the gauge length were manufactured from materials (A) to (E). The specimens were water-jet cut to the geometry as specified in Fig. A.1a. Introduce the Cartesian co-ordinate system such that the load F is applied the axial, x-direction, y is the transverse direction and z is the through-thickness direction. The tensile test was performed using a screw-driven test machine, and the axial extension over the gauge length of the specimen were measured by a laser extensometer. The $\pm 45°$ tensile tests were performed at an axial strain rate in the range $\dot{\varepsilon}_{xx} = 5 \times 10^{-5}$ s^{-1} to 0.13 s^{-1}. The in-plane shear stress τ within each ply is given by

$$\tau = \frac{\sigma_{xx}}{2} = \frac{F}{2wt} \tag{A.1}$$

while the in-plane shear strain γ is related to the tensile strain ε_{xx} and transverse strain ε_{yy} according to

$$\gamma = \varepsilon_{xx} - \varepsilon_{yy} = 2\varepsilon_{xx} \tag{A.2}$$

Representative plots of the in-plane shear stress-strain response of materials (A) to (E) are given in Fig. A.2 for a shear strain rate of $\dot{\gamma} = 1 \times 10^{-3} \text{s}^{-1}$. The ASTM standard D3518 recommends that the in-plane shear yield strength τ_y is defined as the shear flow stress at γ = 5%. The measured values of $\tau_y \equiv \tau(\gamma = 5\%)$ are plotted as a function of shear strain rate $\dot{\gamma}$ in Fig. A3a for materials (A) and (B) and in Fig. A.3b for materials (C) to (E). For completeness, values of flow strength τ at γ = 2.5%, 5%, and 10% are included as a function of shear strain rate $\dot{\gamma}$ in Fig. A.3a.

The data in Fig. A.3a supports the power-law relation in (1), and the exponent m serves as a useful measure of the strain rate sensitivity. The degree of strain rate sensitivity decreases with increasing state of cure. The rate-dependent parameters (τ_0, $\dot{\gamma}_0$ and m) in materials (A) to (B) are summarised in Table 1 with τ_0 defined to be the flow stress $\tau(\gamma = 5\%)$ at $\dot{\gamma}_0 = 10^{-3} s^{-1}$. Materials (C) to (E) yield in an almost rate insensitive manner and the in-plane (IP) flow stress τ_{IP} at $\gamma = 5\%$ is included in Table 1.

A.2 Short Beam Shear Test

The specimens were subjected to out-of-plane shear as follows. Rectangular beams were manufactured from materials (A) to (E), with $[0/90]_{16}$ lay-up, and of beam height H = 4 mm (32 plies), breadth B = 12 mm, and length $2L$ = 25 mm. The beams were tested in three-point bending in accordance with the ASTM standard D2344, as illustrated in Fig. A1b. The three-point bending test made use of a single top roller of diameter of D = 6 mm and two bottom rollers of diameter D = 3 mm, and of span L_s = 5 mm (as defined by the centre-to-centre distance between the top and bottom rollers in the *x*-direction in the figure). The specimens were orientated such that the 0° fibres in the top ply were parallel to the *x*-direction. The short beam shear test was performed such that the top roller moved in the *z*-direction at a displacement rate in the range 0.005 mms^{-1} to 5 mms^{-1}. The deflection of the beams δ during the test was measured using a laser extensometer. The maximum shear stress τ is located at the centre of the beam in the *x*-*z* plane of the figure, and is given by:

$$\tau = \frac{3F}{4BH} \tag{A.3}$$

Assuming a state of shear deformation, the out-of-plane shear strain γ can be expressed as:

$$\gamma = \frac{\delta}{L_s} \tag{A.4}$$

Fig. A.2 provides some examples of the short beam shear stress-strain responses of materials (A) to (E) at a shear strain rate of $\dot{\gamma} = 1 \times 10^{-3} \text{s}^{-1}$. Materials (A) and (B) underwent plastic flow while materials (C) to (E) behaved in an elastic-brittle manner, and failed at $\gamma \sim 5\%$. The measured short beam shear strength is plotted as a function of shear strain rate $\dot{\gamma}$ in Fig. A.3a for materials A and B, and in Fig. A.3b for materials C, D and E.

The short beam shear strength is defined to be $\tau\left(\gamma = 5\%\right)$ for materials (A) and (B) and to be the peak shear stress for materials (C) to (E). As already noted from the $\pm 45°$ tensile test, materials (A) to (B) showed strain rate sensitivity while materials (C) to (E) were almost strain rate insensitive. Furthermore, the rate-dependent parameters (τ_0, $\dot{\gamma}_0$, and m) of materials (A) and (B) as measured from the short beam shear test were the same as those measured by the $\pm 45°$ tensile test. In contrast, for materials (C) to (E), the out-of-plane (OP) shear strength in the short beam shear test differs from the in-plane shear strength as measured by the $\pm 45°$ tensile test. The short beam shear strengths τ_{OP} of materials (C) to (E) are summarised in Table 1 alongside the results from the $\pm 45°$ tensile test.

FIGURE CAPTIONS

Fig. 1. (a) the indirect tension mechanism in a pair of $0°$ and $90°$ plies under out-of-plane pressure; (b) geometry of the quasi-static out-of-plane compression test; and (c) a free-body diagram of a section of the specimen in the $x_2 - x_3$ plane of a $90°$ ply, within the shear lag zone near the periphery of the specimen.

Fig. 2. Mean pressure $\bar{p}$ versus out-of-plane compressive strain $-\varepsilon_{zz}$ for (a) material (A); (b) material (B); (c) material (C); (d) material (D); and (e) material (E) for selected values of side length L; (f) collected results for all five materials for L = 7 mm. All tests were performed at $-\dot{\varepsilon}_{zz} = 8\times10^{-4}\text{s}^{-1}$.

Fig. 3. Average failure pressure $\bar{p}_f$ versus specimen side length L for (a) material (A); (b) material (B); (c) material (C); (d) material (D); and (e) material (E). In each case, tests were performed at 3 selected values of strain rate. (f) Plot of $\bar{p}_f$ versus τ_{OP} at $\dot{\gamma}_0 = 10^{-3}\text{s}^{-1}$ for the five materials of side length L = 7 mm.

Fig. 4. Pressure distribution on top face of a L = 10 mm specimen, for a peak pressure at the centre of the specimen $p_{\max}$ = 250 MPa, and a strain rate of $-\dot{\varepsilon}_{zz} = 8\times10^{-4}\text{s}^{-1}$. (a) measured contours and (b) FE predictions for materials A; (c) measured contours and (d) FE predictions for materials B; (e) measured contours and (f) FE predictions for materials E.

Fig. 5. Pressure profile of a L = 10 mm specimen along the centre line (y = 0) for (a) material (A); (b) material (B); (c) material (C); and (d) material (E) for selected values of $p_{\max}$ (L = 10 mm and $-\dot{\varepsilon}_{zz} = 8\times10^{-4}\text{s}^{-1}$). The solid lines are measurements from pressure sensitive films while the dashed lines represent the FE predictions.

Fig. 6. SEM views of cross-ply specimens of L = 7 mm, with 0.5 mm vertical markings, tested at $-\dot{\varepsilon}_{zz} = 8\times10^{-4}\text{s}^{-1}$ to a compressive strain of $-\varepsilon_{zz}$ =12%. Views of material (A) are (a) side view and (b) top view; views of material (B) are (c) side view and (d) top view; views of material (E) are (e) side view and (f) top view; (g) sketch of the deformed specimens.

Fig. 7. Finite element model. (a) unit cell equal to a quarter of a specimen (with size L /2 x L /2) comprising a single $0°$ ply adhered to an underlying $90°$ ply. Periodic boundary conditions are prescribed at the top and bottom surfaces in the stack of $0°$ and $90°$ plies. (b) Top view of the FE model with quarter symmetry enforced along the centre lines. (c) A single ply consisting of one core layer of height H sandwiched between two inter-layers of height h.

Fig. 8. (a) Normalised stress components σ_{22}/τ_y and σ_{33}/τ_y at yield of CFRP UD plies and GFRP UD plies, subjected to out-of-plane compression with superimposed hydrostatic pressure. Data of CFRP were obtained from Pae and Rhee (1995) and Hine et al. (1999). Data of GFRP were obtained from Parry and Wronski (1990) and Hine et al. (2005). (b) Plot of normalised stress components σ_{11}/S_L^+ and $\sigma_{22}/S_L^+ = \sigma_{33}/S_L^+$ at ply tensile failure of a UD composite ply subjected to in-plane tension with superimposed hydrostatic pressure. Data of CFRP were obtained from Parry and Wronski (1985) and Hine et al. (1999). Data of GFRP were obtained from Parry and Wronski (1986) Sigley et al. (1991), and Hine et al. (1999). Data of Kevlar® composites were obtained from Zinoviev and Tsvetkov (1998) and Hine et al. (2005).

Fig. 9. Average pressure $\overline{p}$ versus compressive strain $-\varepsilon_{zz}$ of (a) material (A); (b) material (C); and (e) material (E) at a strain rate of $-\dot{\varepsilon}_{zz} = 8\times10^{-4}\text{s}^{-1}$. Solid lines represent the data measured from the experiments and dashed lines represent the FE predictions.

Fig. A.1. Sketches of (a) a $\pm45°$ dog-bone specimen for tensile test and (b) a short beam shear test specimen. All dimensions are in mm.

Fig. A.2. A comparison of the shear stress versus shear strain responses for the short beam shear test and the tension test on a $\pm45°$ specimen at a shear strain rate of $\dot{\gamma}_0 = 1\times10^{-3}\text{s}^{-1}$. (a) material (A); (b) material (B); (c) material (C); and (d) materials (D) and (E).

Fig. A.3. In-plane shear strength τ_{IP} and out-of-plane longitudinal shear strength τ_{OP} versus strain rate $\dot{\gamma}$ for (a) materials (A) and (B) and (b) for materials (C) to (E).

TABLE CAPTIONS

Table 1. Shear test results measured from CFRP laminates in various states of cure.

Table 2. The geometrical parameters and material properties used in the FE and analytical models.

Table 1. Shear test results measured from CFRP laminates in various states of cure.

Material	Reference strain rate $\dot{\gamma}_0$ (s^{-1})	Reference shear stress τ_0 (MPa)	Strain rate sensitivity coefficient m	In-plane shear stress τ_{IP} (MPa)	Out-of-plane longitudinal shear stress τ_{OP} (MPa)
A	10^{-3}	0.11	0.45	--	--
B	10^{-3}	0.82	0.39	--	--
C	--	--	--	48 ± 2.3	22 ± 1.9
D	--	--	--	87 ± 8.2	61 ± 3.7
E	--	--	--	87 ± 0.85	99 ± 6.9

Table 2. The geometrical parameters and material properties as used in the FE and analytical models.

Materials	A	B	C	D	E
Thickness of core layer H (μm)	129	129	129	129	129
Thickness of inter-layer h (μm)	1	1	1	1	1
Reference strain rate $\dot{\varepsilon}_0^{(IP)}$, $\dot{\varepsilon}_0^{(OP)}$ (s^{-1})	5×10^{-4}	5×10^{-4}	5×10^{-4}	5×10^{-4}	5×10^{-4}
Core layer reference stress $\sigma_0^{(IP)}$ (MPa)	0.22	1.64	96	174	174
Inter-layer reference stress $\sigma_0^{(OP)}$ (MPa)	0.22	1.64	44	122	198
Strain rate dependency m	0.45	0.39	0	0	0
Matrix pressure dependency μ	0.05	0.2	0.2	0.2	0.2
In-plane modulus E_1 (GPa) [1]	164	164	164	164	164
Transverse modulus E_3 (GPa) [1]	10	10	10	10	10
Shear modulus G_{12} (GPa) [2]	5	5	5	5	5
Poisson's ratio ν_{23} [2]	0.43	0.43	0.43	0.43	0.43
Poisson's ratio ν_{31} [2]	0.02	0.02	0.02	0.02	0.02
Ply tensile strength S_L^+ (GPa) [2]	2.7	2.7	2.7	2.7	2.7
Tensile strength pressure dependency α	2	2	2	2	2

[1] Data obtained from Hexcel Composites (2013)
[2] Data obtained from Marlett (2011)

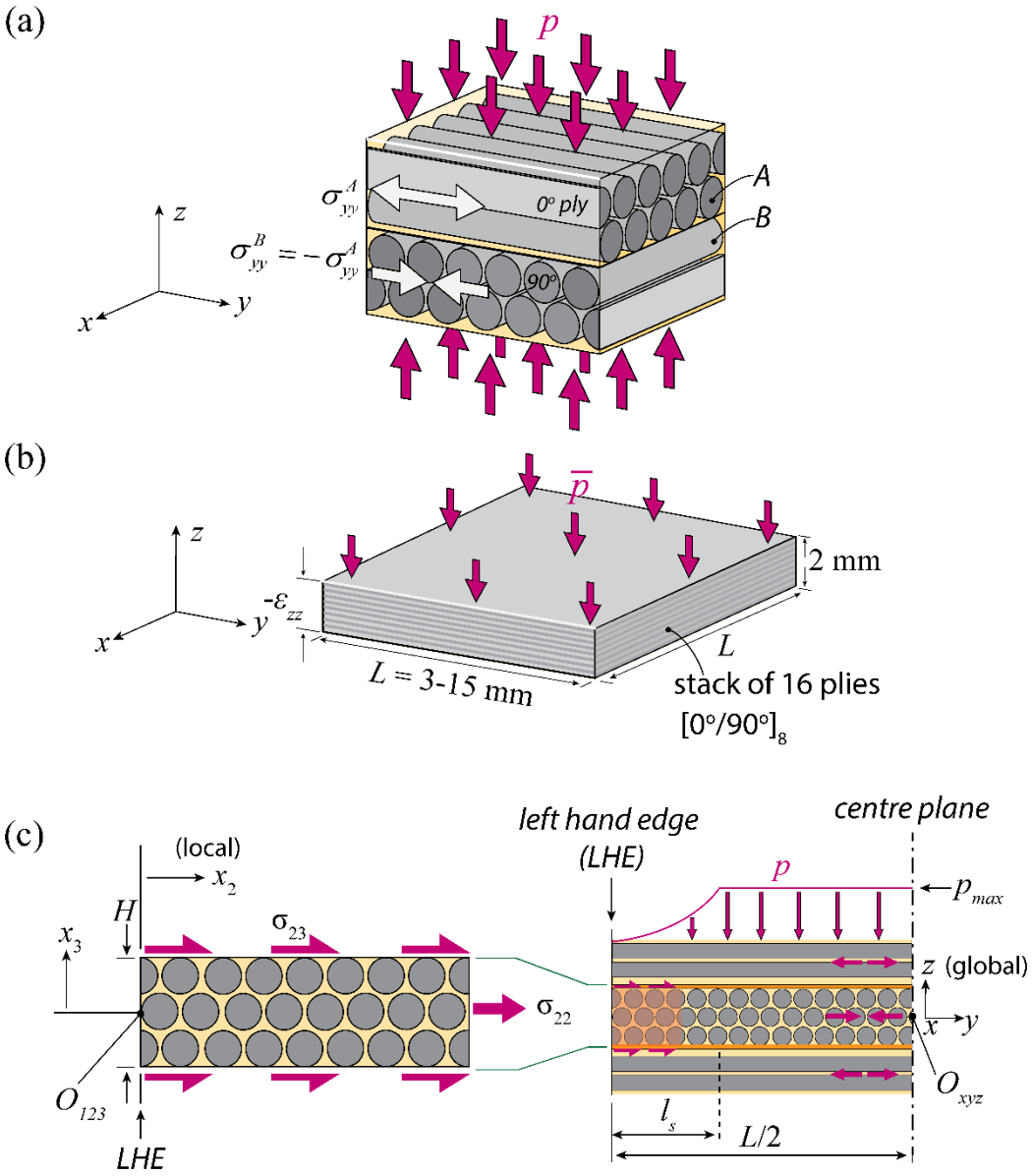

Fig. 1. (a) the indirect tension mechanism in a pair of 0° and 90° plies under out-of-plane pressure; (b) geometry of the quasi-static out-of-plane compression test; and (c) a free-body diagram of a section of the specimen in the $x_2 - x_3$ plane of a 90° ply, within the shear lag zone near the periphery of the specimen.

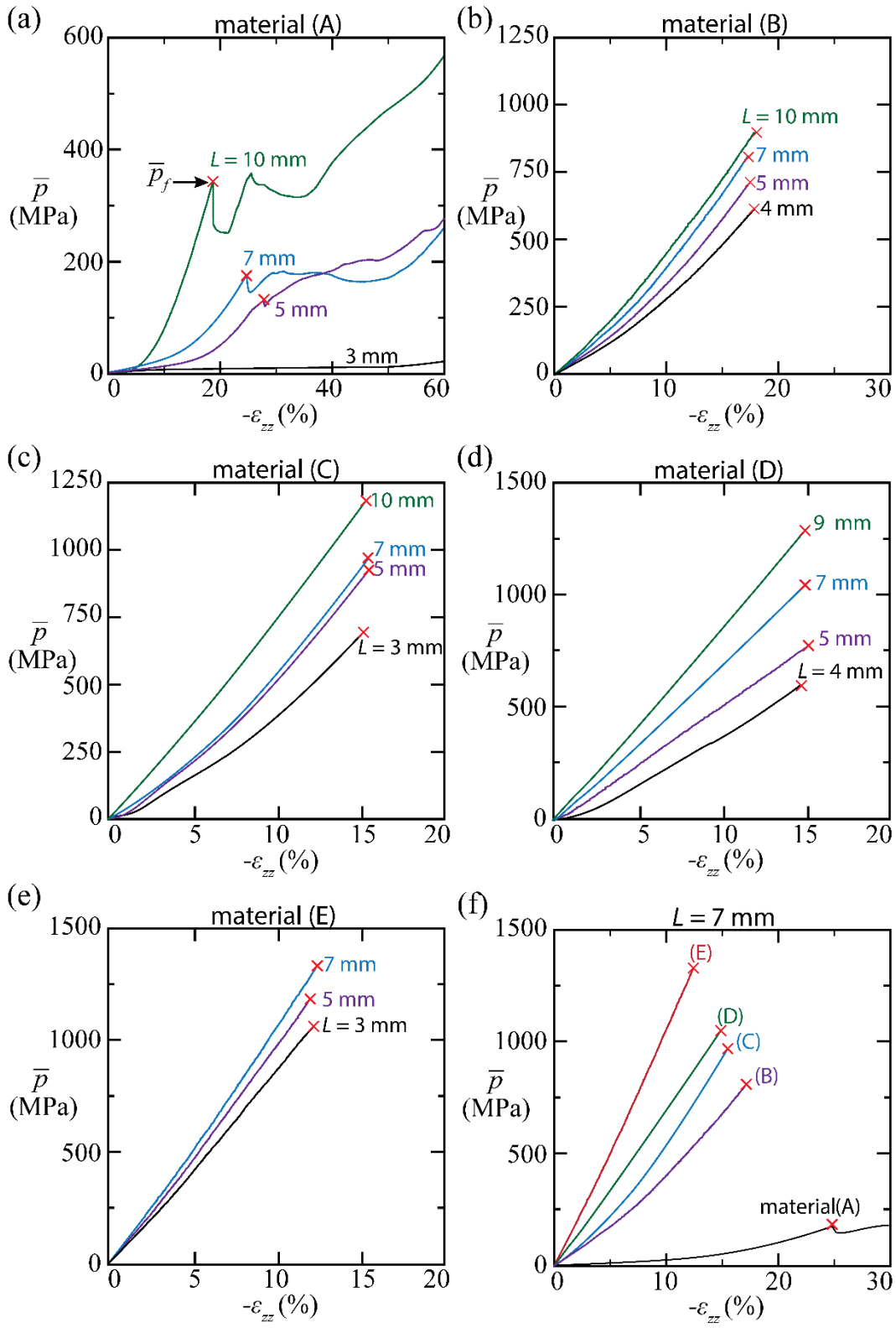

Fig. 2. Mean pressure $\bar{p}$ versus out-of-plane compressive strain $-\varepsilon_{zz}$ for (a) material (A); (b) material (B); (c) material (C); (d) material (D); and (e) material (E) for selected values of side length L; (f) collected results for all five materials for L = 7 mm. All tests were performed at $-\dot{\varepsilon}_{zz} = 8\times10^{-4}\text{s}^{-1}$.

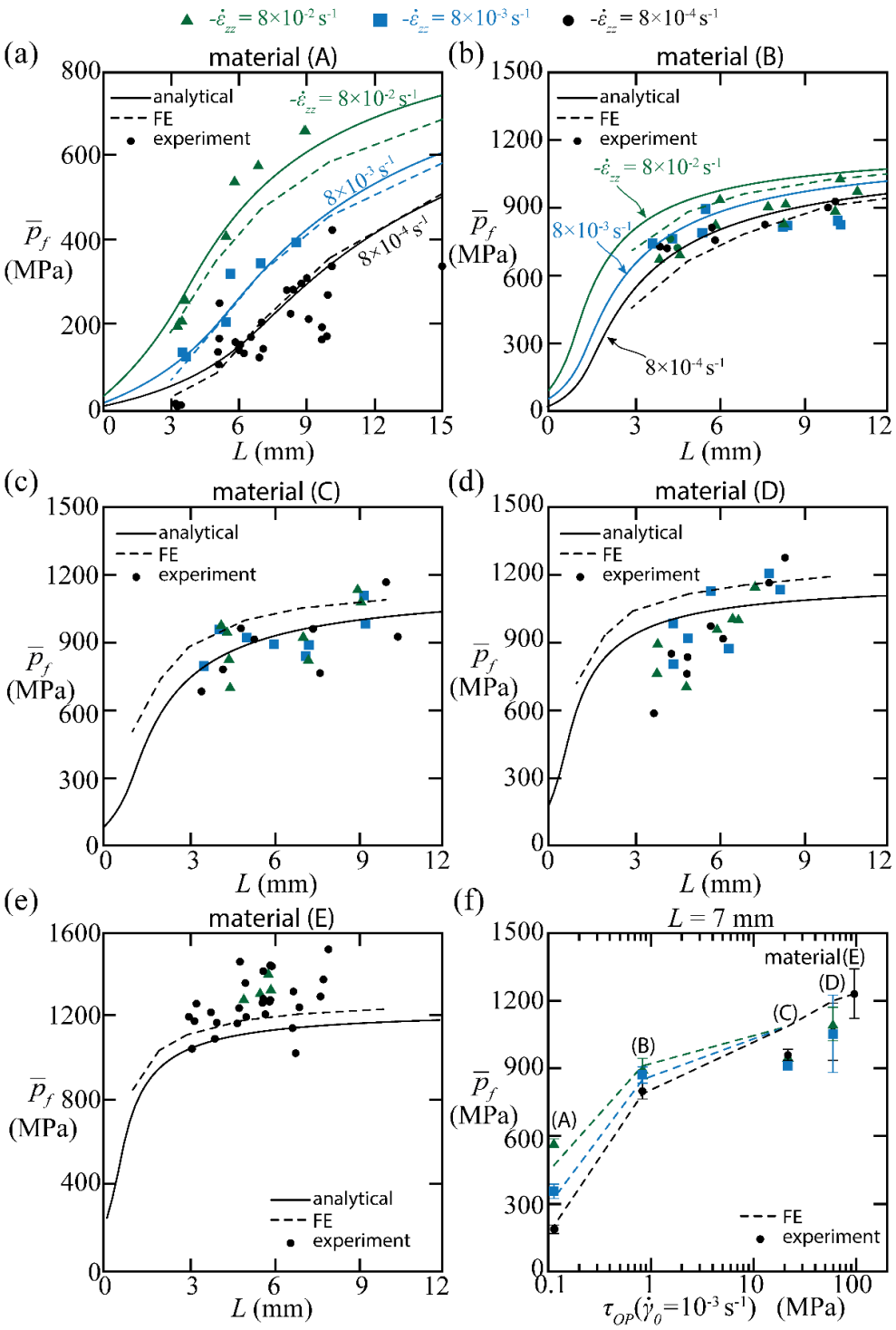

Fig. 3. Average failure pressure $\overline{p}_f$ versus specimen side length L for (a) material (A); (b) material (B); (c) material (C); (d) material (D); and (e) material (E). In each case, tests were performed at 3 selected values of strain rate. (f) Plot of $\overline{p}_f$ versus τ_{OP} at $\dot{\gamma}_0 = 10^{-3}\,s^{-1}$ for the five materials of side length L = 7 mm.

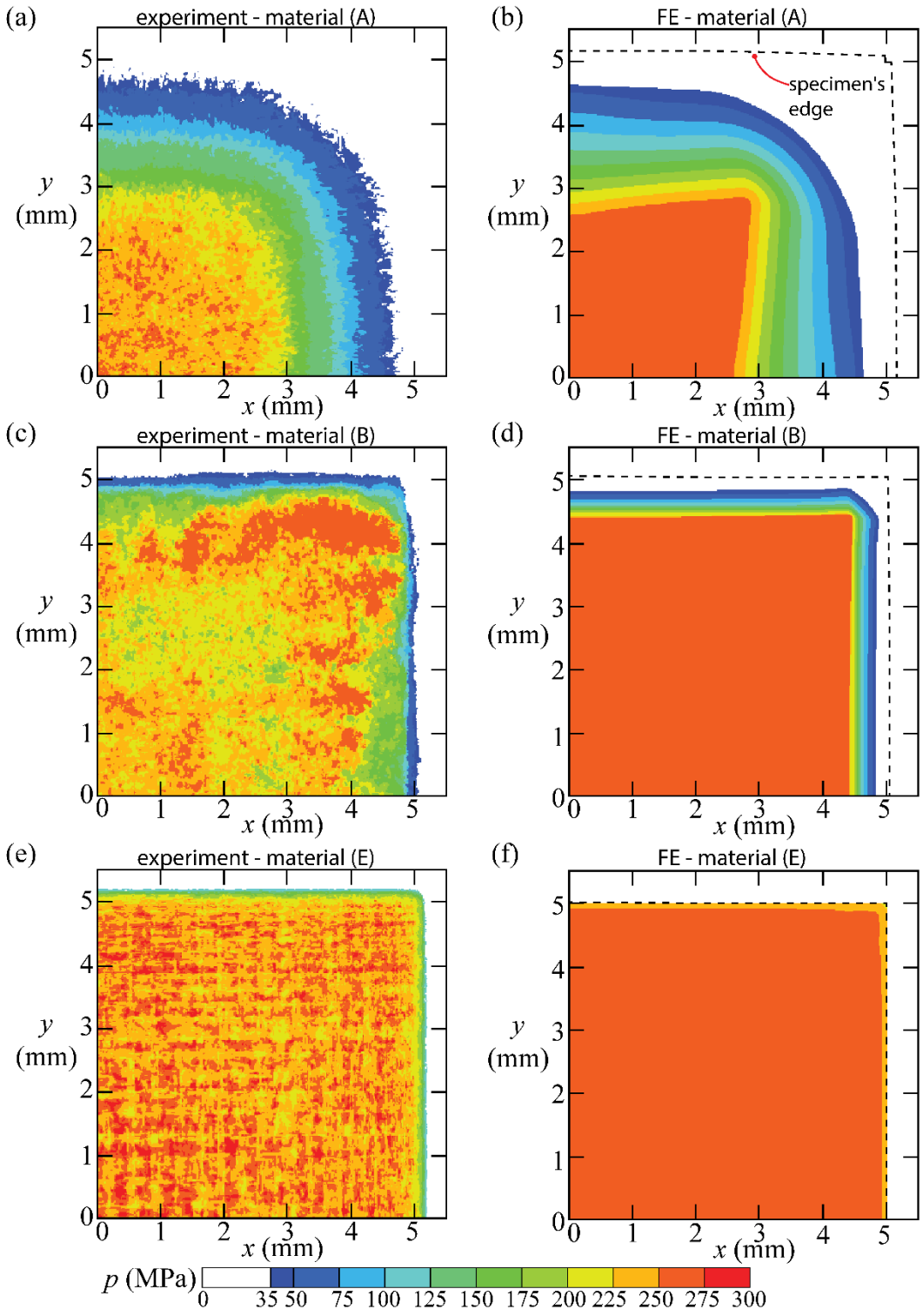

Fig. 4. Pressure distribution on top face of a L = 10 mm specimen, for a peak pressure at the centre of the specimen p_{max} = 250 MPa, and a strain rate of $-\dot{\varepsilon}_{zz} = 8\times10^{-4}\text{s}^{-1}$. (a) measured contours and (b) FE predictions for materials A; (c) measured contours and (d) FE predictions for materials B; (e) measured contours and (f) FE predictions for materials E.

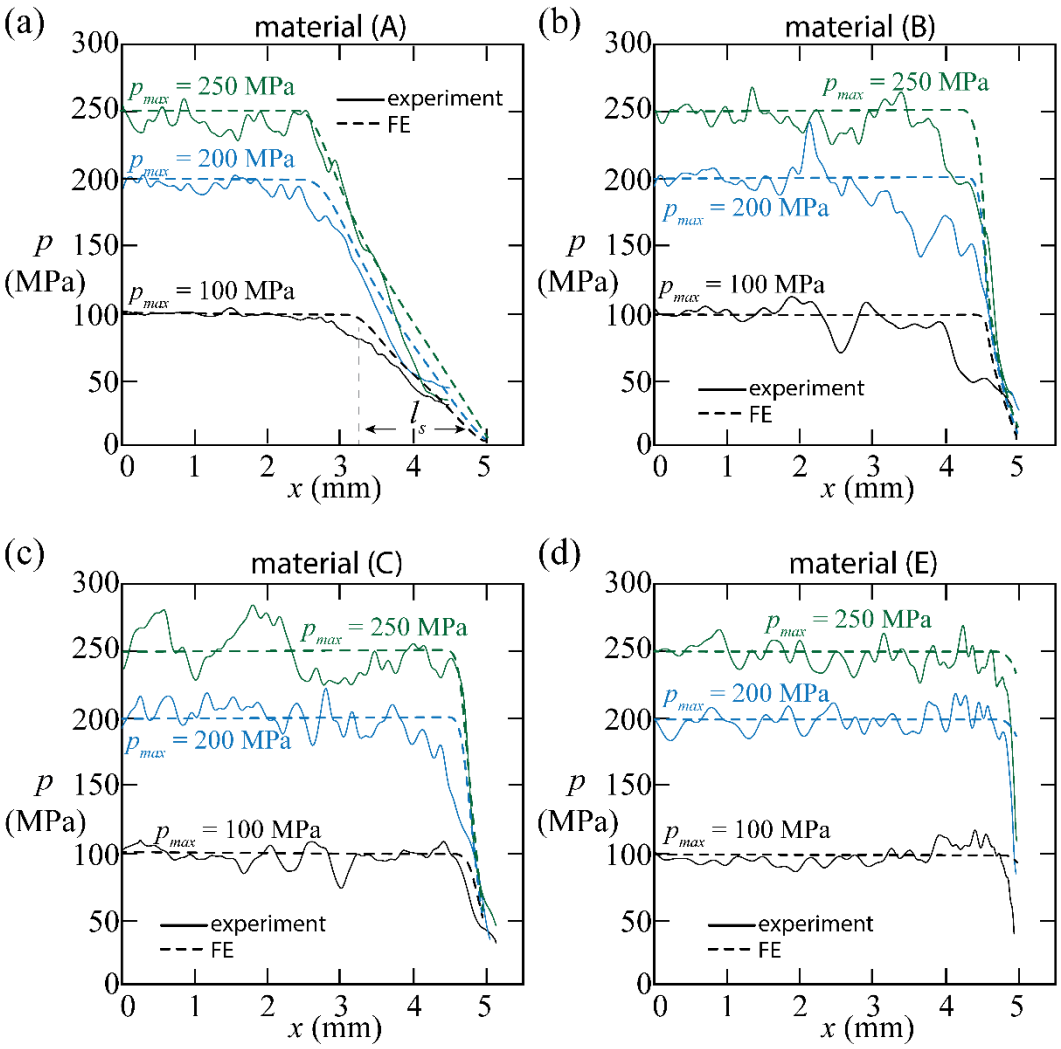

Fig. 5. Pressure profile of a L = 10 mm specimen along the centre line (y = 0) for (a) material (A); (b) material (B); (c) material (C); and (d) material (E) for selected values of $p_{\max}$ (L = 10 mm and $-\dot{\varepsilon}_{zz} = 8\times10^{-4}\text{s}^{-1}$). The solid lines are measurements from pressure sensitive films while the dashed lines represent the FE predictions.

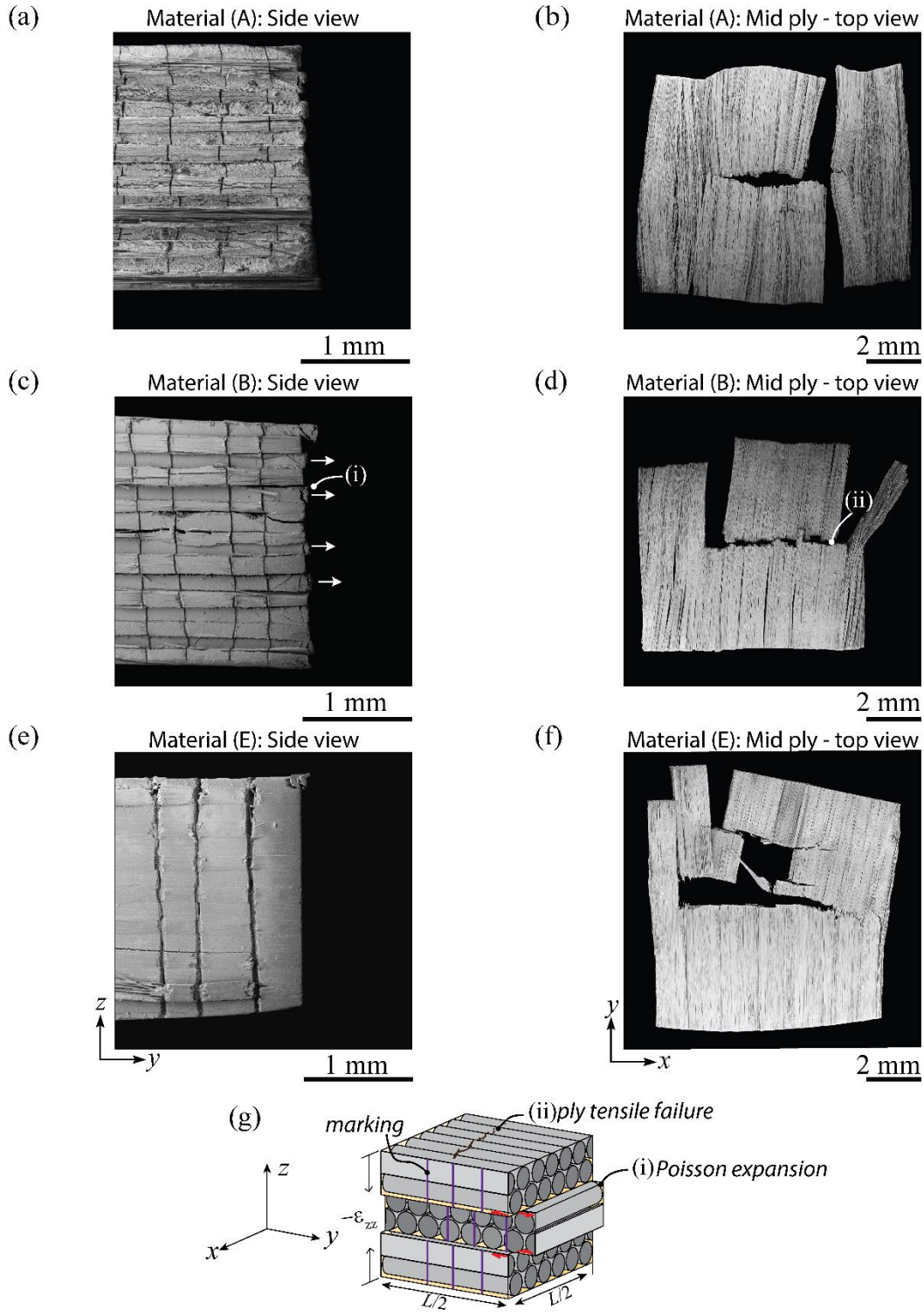

Fig. 6. SEM views of cross-ply specimens of L = 7 mm, with 0.5 mm vertical markings, tested at $-\dot{\varepsilon}_{zz} = 8\times10^{-4}\text{s}^{-1}$ to a compressive strain of $-\varepsilon_{zz}$ =12%. Views of material (A) are (a) side view and (b) top view; views of material (B) are (c) side view and (d) top view; views of material (E) are (e) side view and (f) top view; (g) sketch of the deformed specimens.

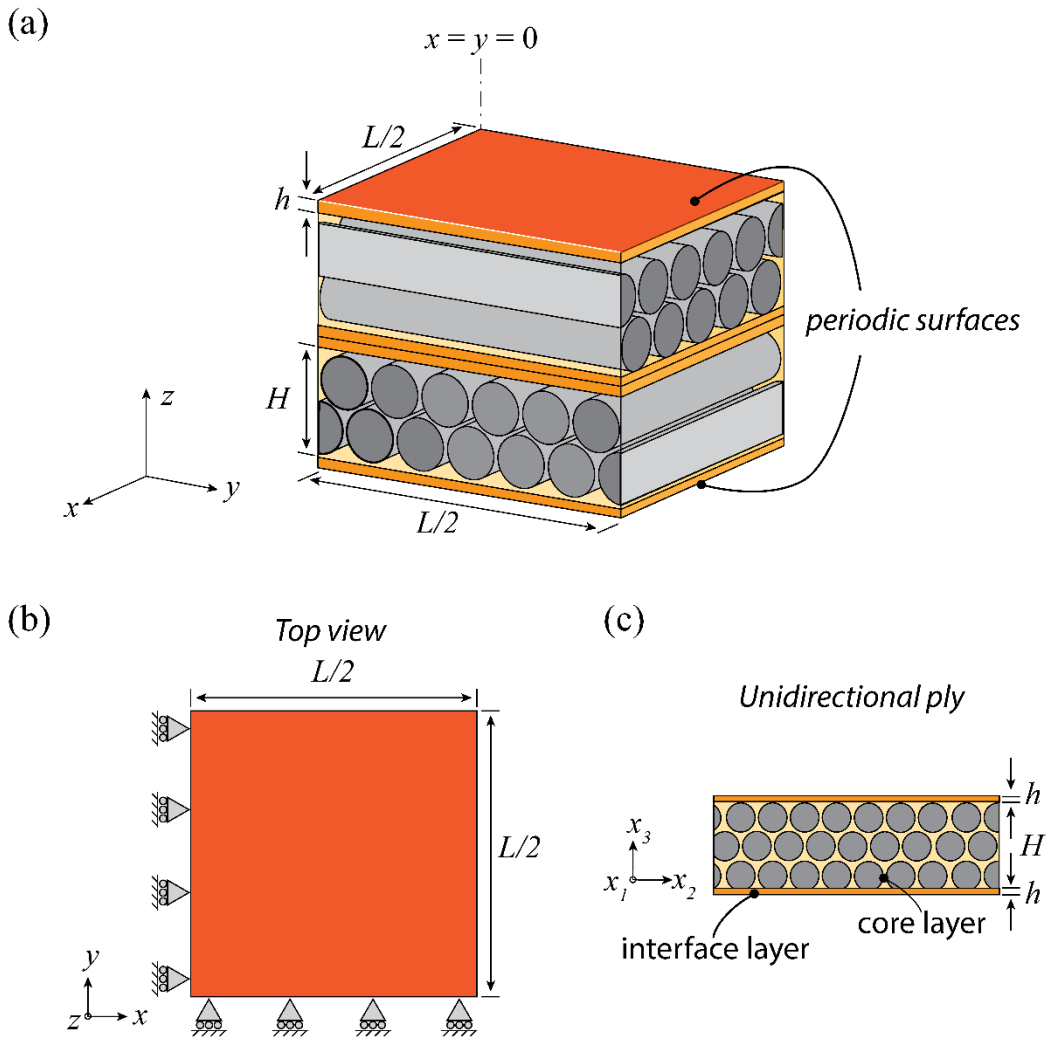

Fig. 7. Finite element model. (a) unit cell equal to a quarter of a specimen (with size L /2 x L /2) comprising a single $0°$ ply adhered to an underlying $90°$ ply. Periodic boundary conditions are prescribed at the top and bottom surfaces in the stack of $0°$ and $90°$ plies. (b) Top view of the FE model with quarter symmetry enforced along the centre lines. (c) A single ply consisting of one core layer of height H sandwiched between two inter-layers of height h.

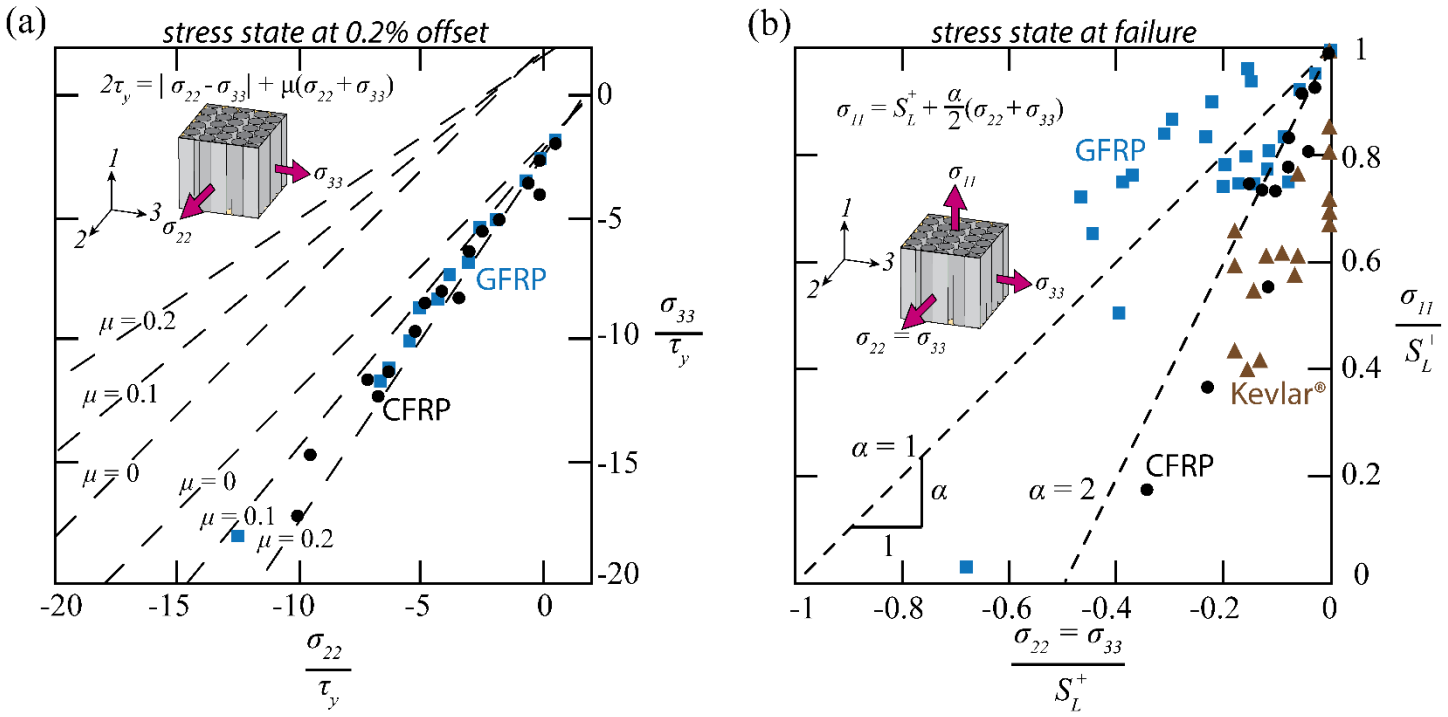

Fig. 8. (a) Normalised stress components σ_{22}/τ_y and σ_{33}/τ_y at yield of CFRP UD plies and GFRP UD plies, subjected to out-of-plane compression with superimposed hydrostatic pressure. Data of CFRP were obtained from Pae and Rhee (1995) and Hine et al. (1999). Data of GFRP were obtained from Parry and Wronski (1990) and Hine et al. (2005). (b) Plot of normalised stress components σ_{11}/S_L^+ and $\sigma_{22}/S_L^+ = \sigma_{33}/S_L^+$ at ply tensile failure of a UD composite ply subjected to in-plane tension with superimposed hydrostatic pressure. Data of CFRP were obtained from Parry and Wronski (1985) and Hine et al. (1999). Data of GFRP were obtained from Parry and Wronski (1986) Sigley et al. (1991), and Hine et al. (1999). Data of Kevlar® composites were obtained from Zinoviev and Tsvetkov (1998) and Hine et al. (2005).

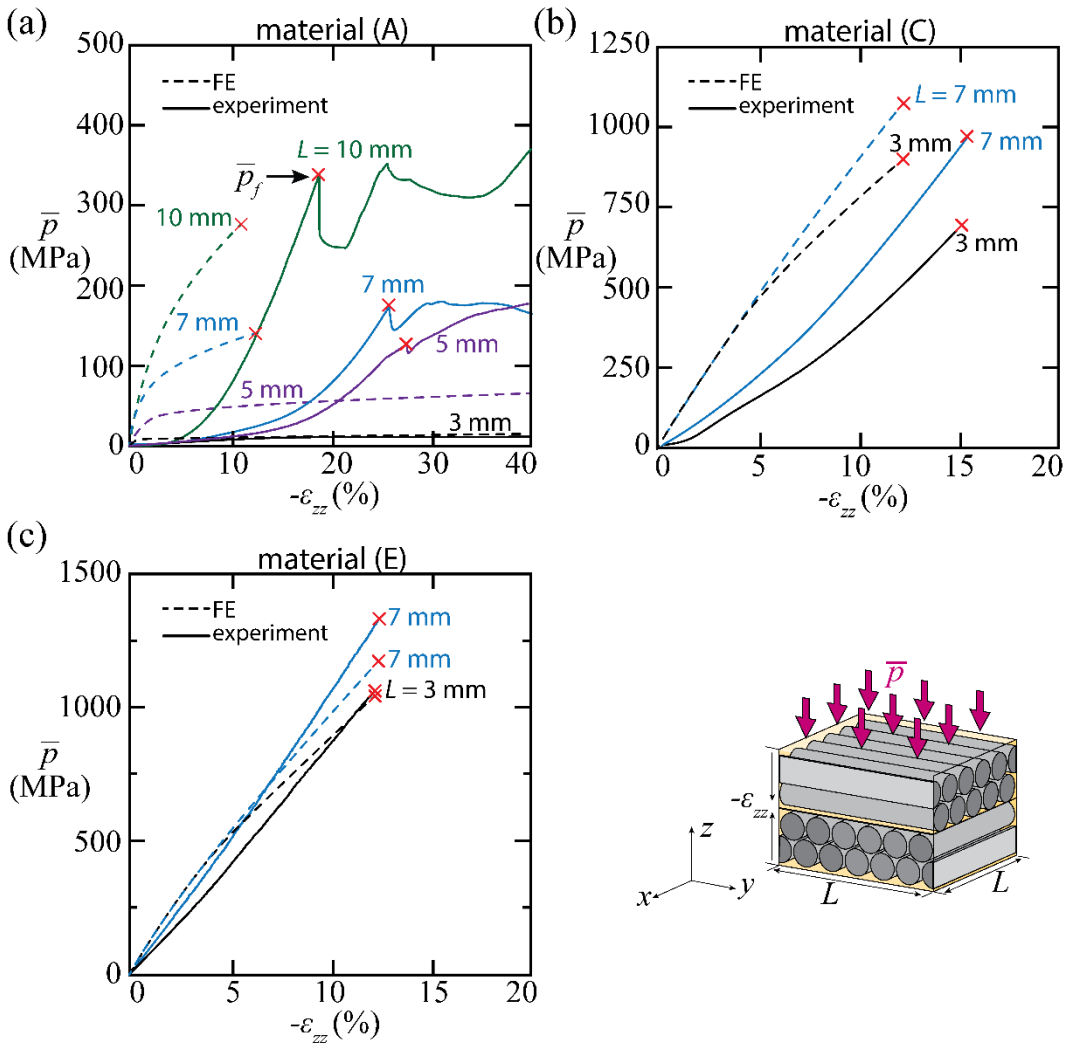

Fig. 9. Average pressure $\overline{p}$ versus compressive strain $-\varepsilon_{zz}$ of (a) material (A); (b) material (C); and (e) material (E) at a strain rate of $-\dot{\varepsilon}_{zz} = 8\times10^{-4}\text{s}^{-1}$. Solid lines represent the data measured from the experiments and dashed lines represent the FE predictions.

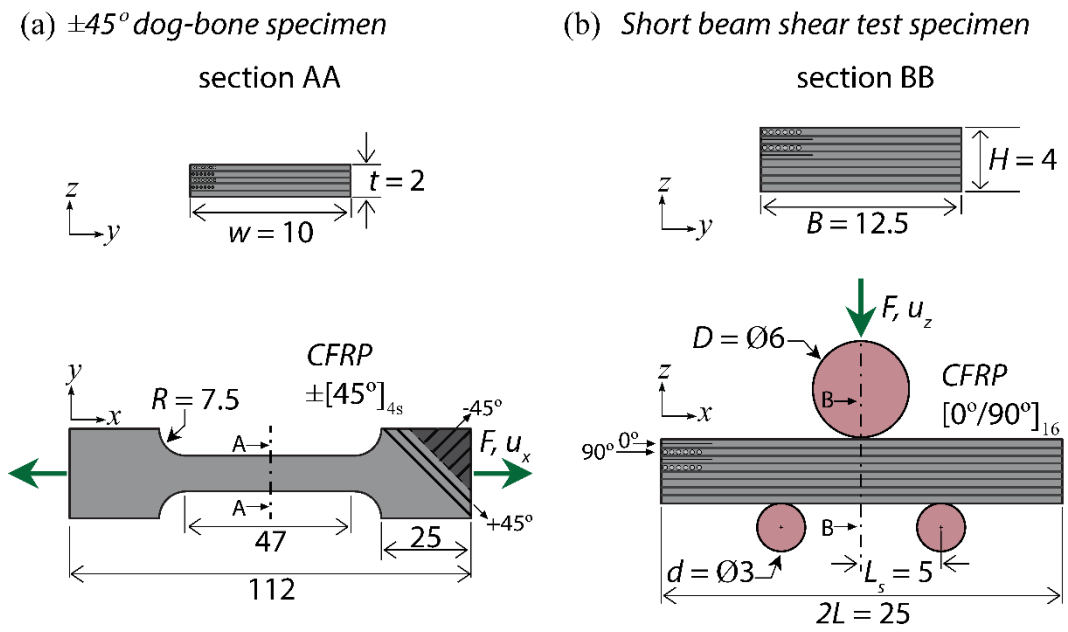

Fig. A.1. Sketches of (a) a ±45° dog-bone specimen for tensile test and (b) a short beam shear test specimen. All dimensions are in mm.

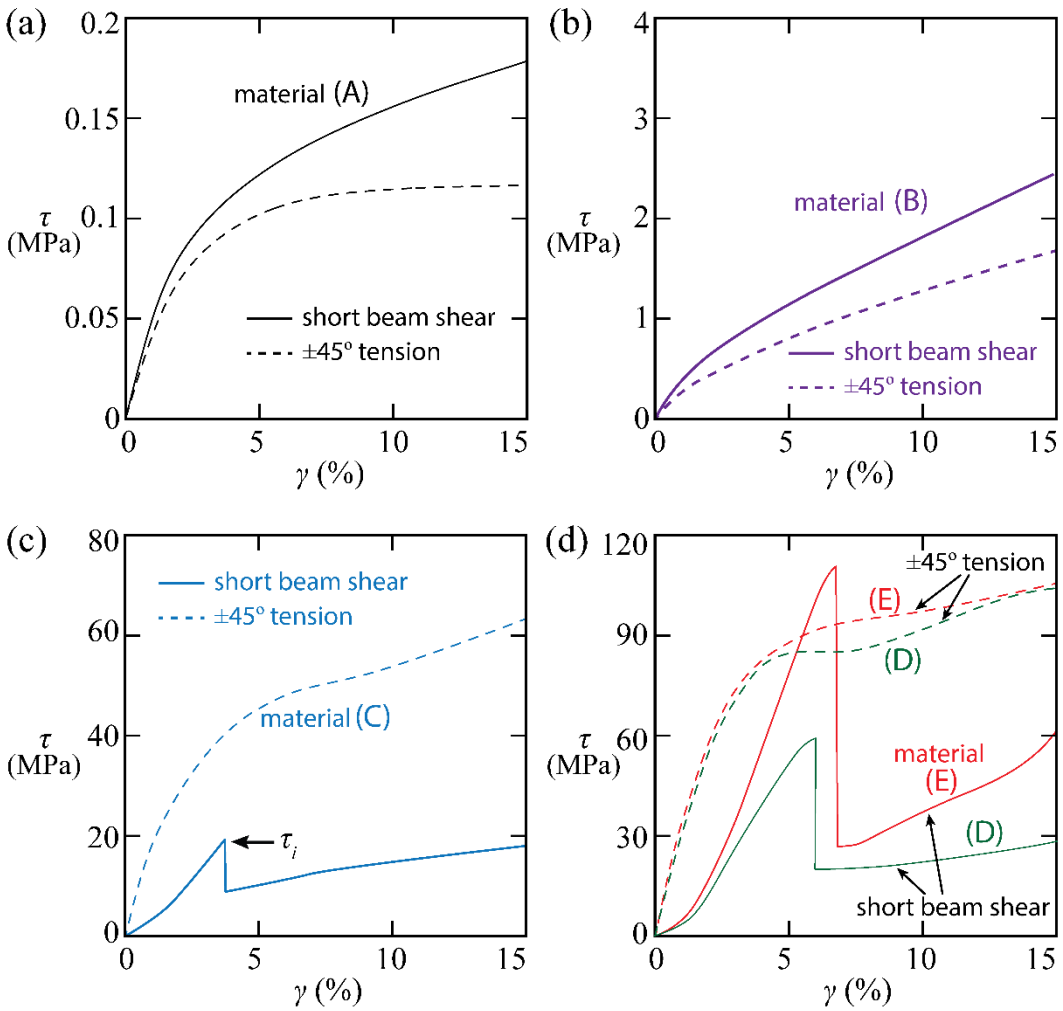

Fig. A.2. A comparison of the shear stress versus shear strain responses for the short beam shear test and the tension test on a $\pm 45°$ specimen at a shear strain rate of $\dot{\gamma}_0 = 1\times10^{-3}\text{s}^{-1}$. (a) material (A); (b) material (B); (c) material (C); and (d) materials (D) and (E).

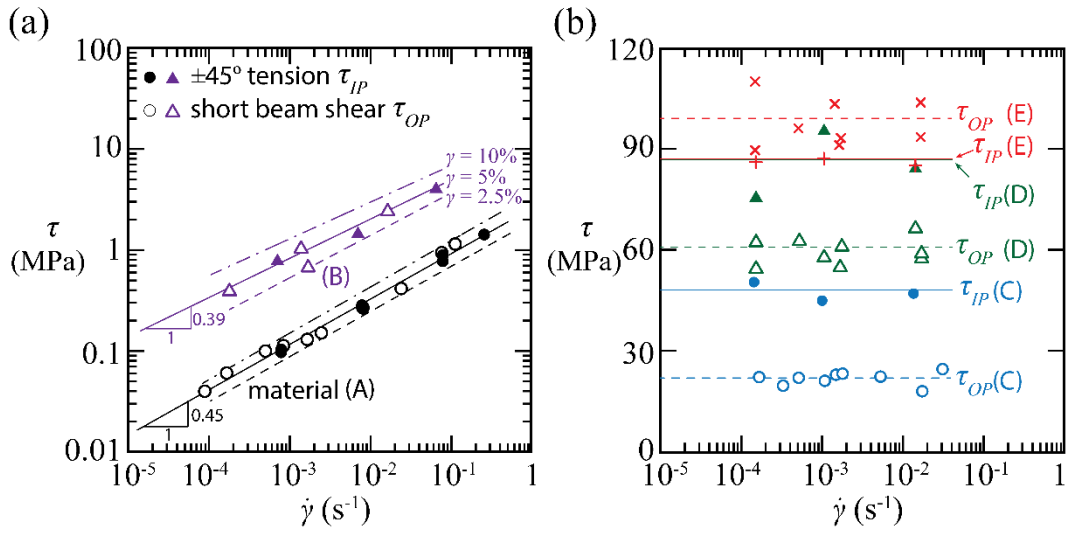

Fig. A.3. In-plane shear strength τ_{IP} and out-of-plane longitudinal shear strength τ_{OP} versus strain rate $\dot{\gamma}$ for (a) materials (A) and (B) and (b) for materials (C) to (E).